



**HAL**  
open science

# Étude comparative de deux méthodes de lissage pour les simulations de contact avec grands glissements

Alain Batailly, Benoit Magnain, Nicolas Chevaugéon

## ► To cite this version:

Alain Batailly, Benoit Magnain, Nicolas Chevaugéon. Étude comparative de deux méthodes de lissage pour les simulations de contact avec grands glissements. *Computational Mechanics*, 2012, pas encore disponible. 10.1007/s00466-012-0737-3 . hal-00711088v1

**HAL Id: hal-00711088**

**<https://hal.science/hal-00711088v1>**

Submitted on 22 Jun 2012 (v1), last revised 22 Jun 2012 (v2)

**HAL** is a multi-disciplinary open access archive for the deposit and dissemination of scientific research documents, whether they are published or not. The documents may come from teaching and research institutions in France or abroad, or from public or private research centers.

L'archive ouverte pluridisciplinaire **HAL**, est destinée au dépôt et à la diffusion de documents scientifiques de niveau recherche, publiés ou non, émanant des établissements d'enseignement et de recherche français ou étrangers, des laboratoires publics ou privés.

# Étude comparative de deux méthodes de lissage pour les simulations de contact avec grands glissements

A. Batailly, Laboratoire de dynamique des structures et vibrations, Université McGill, Montréal, Québec

B. Magnain, Laboratoire PRISME, ENSI de Bourges, France

N. Chevaugéon, Gém, École Centrale Nantes, France

Cet article est initialement paru dans la revue **Computational Mechanics**. Au texte original en anglais, est ajouté un bref résumé en français des travaux.

---

**Résumé :** *La simulation numérique des problèmes de contact comporte de nombreuses difficultés, notamment lorsqu'on considère de grands déplacements et de grandes déformations. Les grands glissements relatifs pouvant alors se produire entre les surfaces de contact ainsi que les erreurs de discrétisation peuvent aboutir à des résultats insatisfaisants. En particulier, les éléments finis usuels impliquent une facettisation de la surface de contact ce qui entraîne inévitablement la discontinuité de l'orientation du vecteur normale à la surface de contact. Les conséquences d'une telle discontinuité peuvent être : des résultats imprécis, des déplacements non réguliers, ou encore des oscillations numériques des efforts de contact calculés. Il existe plusieurs méthodes permettant de résoudre ces problèmes parmi lesquelles : les éléments de type mortar [1, 2, 3], les méthodes de lissage de la surface de contact par ajout d'une entité géométrique (type B-spline ou NURBS) [4, 5, 6, 7, 8], ainsi que les analyses de type iso-géométriques [9, 10, 11]. Les travaux présentés dans cet article portent sur les deux derniers types de méthodes qui sont utilisées en combinaison avec un algorithme de traitement du contact avec la méthode du bi-potentiel [12]. Une étude comparative des avantages et inconvénients de chaque méthode en termes de précision géométrique et de stabilité de la solution du problème de contact associé. Plusieurs cas tests sont étudiés pour illustrer cette comparaison.*

---

## 1 Introduction

Les problèmes de contact sont intrinsèquement non-linéaires du fait que la surface de contact est inconnue *a priori*. Usuellement, trois méthodes sont utilisées dans le cadre de la méthode éléments finis pour traiter des problèmes de contact: (1) la méthode de pénalité [13, 6], (2) la méthode des multiplicateurs de Lagrange [14, 15] et, (3) la méthode du Lagrangien augmenté [16, 17, 18]. La simplicité d'implémentation de la méthode de pénalité est malheureusement contre-balançée par le fait qu'elle permet, par construction, des pénétrations entre les structures. Inversement, les multiplicateurs de Lagrange, qui représentent les réactions de contact, permettent de respecter les conditions de non pénétrabilité mais peuvent s'avérer coûteux en termes de temps de calculs. La méthode du Lagrangien augmenté permet le respect des conditions de non-pénétrabilité sans avoir à considérer de nouvelles variables.

Les développements présentés dans cet article ont pour but d'être appliqué à l'étude des contacts au sein des turbomachines aéronautiques [19, 20]. La grande sensibilité de ce type de simulations numériques impose notamment un respect très précis des conditions de non pénétrabilité. La méthode de pénalité n'est donc pas utilisable dans notre cas et la méthode du bi-potentiel lui est préférée [12].

## 2 Gestion du contact

Cette section rappelle brièvement les bases théoriques associées au traitement du contact dans le cadre de la méthode des éléments finis. Les notations utilisées sont tout d'abord données dans le cas d'un problème continu (voir équations (1) et (2)) puis l'algorithme utilisé est détaillé pour un problème discret. Les trois principales étapes de cet algorithme sont détaillées sous formes d'organigrammes sur les figures 3, 4 et 6).

## 3 Méthodes de lissage des surfaces de contact

### 3.1 B-splines

De très nombreuses publications [10, 11] existent relativement à la combinaison d'entités géométriques de type B-splines ou NURBS et de maillages éléments finis pour la représentation de surfaces de contact. Récemment, les

NURBS sont devenues plus fréquentes que les B-splines dont un inconvénient majeur est l'impossibilité de représenter parfaitement une surface circulaire. Cependant, lorsque deux structures déformables sont considérées, les surfaces de contact ne sont plus régulières et les B-splines peuvent être particulièrement intéressantes à utiliser. En particulier, les B-splines uniformes permettent de limiter l'augmentation du temps de calcul et c'est essentiellement pour cette raison qu'elles sont utilisées dans notre étude.

Les rappels théoriques concernant les B-splines ne sont pas détaillés ici, pas plus que le soin particulier apporté au choix des conditions limites pour optimiser le profil de la surface de contact.

### 3.2 Éléments de type Hermite

Les éléments de type Hermite sont moins présents dans la littérature scientifique que les courbes paramétriques pour le lissage des surfaces de contact. La particularité des éléments de Hermite est d'intégrer des degrés de liberté associés aux dérivées des degrés de liberté en déplacements usuels afin d'assurer la continuité de la pente de l'arrête de l'élément en passant d'un élément à son voisin. Le comportement d'un tel élément diffère sensiblement du comportement d'autres éléments finis plus fréquemment utilisés, c'est la raison pour laquelle la section 3.2.2 contient un exemple de déformation statique de cet élément (figure 11).

### 3.3 Étude géométrique

à partir d'un demi-anneau encastré à chacune de ses extrémités (figure 12), une étude géométrique est conduite afin d'évaluer l'apport des méthodes de lissage par rapport aux éléments finis usuels (éléments linéaires Q4, éléments quadratiques Q8 et éléments cubiques Q12) pour (1) l'erreur de discrétisation ainsi que pour (2) l'erreur sur le calcul de l'angle de la normale à la surface de contact. Les résultats présentés sur les figures 13 et 14 montrent l'évolution de ces deux quantités lorsque le maillage est raffiné. En termes de précision, les méthodes de lissage sont comparables à un maillage Q8 mais elles permettent surtout de supprimer la discontinuité de l'orientation de la normale à la surface de contact.

## 4 Étude comparative avec grands glissements

En tout, trois cas tests sont proposés dans cette section.

### 4.1 Poutre et demi-anneau

Ce cas test permet essentiellement de valider la procédure de détection utilisée dans l'algorithme de contact. Aucune différence n'est visible entre les résultats obtenus avec un maillage linéaire, et ceux obtenus avec chacune des méthodes de lissage.

### 4.2 Carré entre deux demi-anneaux

Ce cas test est beaucoup plus sévère numériquement que le précédent. Le glissement du carré entre les anneaux et les déformations subies par les anneaux en atteste (figure 16). Il est tout d'abord vérifié que la symétrie du cas de contact se reflète effectivement sur les résultats obtenus (figure 18(b)).

L'analyse des résultats obtenus met en évidence les approximations générées par l'utilisation d'un maillage linéaire. Bien que des différences significatives apparaissent en regardant en détails les résultats obtenus en termes de déplacements et d'efforts de contact, l'utilisation d'un maillage linéaire reste envisageable puisque les oscillations numériques n'empêchent pas les calculs de converger.

### 4.3 Anneaux concentriques

Ce cas test a été initialement proposé dans [4]. Deux anneaux concentriques (nommés *intérieur* et *extérieur*) sont tels que le rayon intérieur de l'anneau extérieur est égal au rayon extérieur de l'anneau intérieur (figure 24). Les deux anneaux sont maillés avec un même nombre d'éléments et, dans un premier temps, un effort est appliqué sur la circonférence extérieure de l'anneau extérieur. Sous l'effet de cet effort, des différences significatives apparaissent

entre les différents maillages comme le montre la figure 25. Une rupture de symétrie apparaît clairement dans le cas du maillage linéaire. Dans un deuxième temps, alors que l'effort appliqué sur l'anneau extérieur est maintenu, l'anneau intérieur tourne d'un angle  $\theta = \pi$ . On s'intéresse alors à la répartition du chargement sur la surface de contact au cours de cette rotation (figures 26(a), 26(b) et 26(c)). Il est mis en évidence que l'ensemble des méthodes considérées aboutit à dissymétrie du chargement sur la surface de contact mais que celle-ci est négligeable lorsque la B-spline ou les éléments de Hermite sont utilisés.

La comparaison des résultats obtenus avec B-splines et éléments de type Hermite met en évidence des différences significatives entre les deux méthodes du fait du comportement particulier des éléments de Hermite. En particulier, une ondulation de la surface de contact est observée avec les éléments de Hermite. Celle-ci ne résulte pas d'une quelconque limitation associée aux éléments de Hermite. Bien au contraire, cette ondulation reflète une limitation associée à l'algorithme noeud/segment utilisé pour le traitement du contact et qui introduit une dissymétrie. Dans le cas de la combinaison du maillage linéaire avec courbe B-spline, cette dissymétrie est filtrée du fait de la répartition des efforts de contact à chaque extrémité des patches splines.

## 5 Conclusion

Cette étude permet de mettre en évidence les différences fondamentales existant entre les deux méthodes de lissage que sont l'ajout d'une entité géométrique de type B-spline et une approche iso-géométrique avec des éléments de Hermite. Chaque méthode permet d'améliorer significativement la précision des simulations réalisées et remplace ainsi avantageusement l'utilisation de maillages avec des éléments d'ordre plus élevés très coûteux du fait de l'ajout de nombreux degrés de liberté. Alors que l'ajout d'une entité géométrique se montre particulièrement efficace lorsque le maillage éléments finis ne peut pas être modifié (par exemple pour une application industrielle), l'utilisation des éléments de Hermite permettent d'atteindre un niveau de précision encore supérieur avec des résultats qui reflètent très précisément le type de formulation utilisée pour la gestion du contact.

# A comparative study between two smoothing strategies for the simulation of contact with large sliding

A. Batailly, Laboratoire de dynamique des structures et vibrations, Université McGill, Montréal, Québec

B. Magnain, Laboratoire PRISME, ENSI de Bourges, France

N. Chevaugéon, Gém, École Centrale Nantes, France

---

**Abstract:** *The numerical simulation of contact problems is still a delicate matter especially when large transformations are involved. In that case, relative large slidings can occur between contact surfaces and the discretization error induced by usual finite elements may not be satisfactory. In particular, usual elements lead to a facetization of the contact surface, meaning an unavoidable discontinuity of the normal vector to this surface. Uncertainty over the precision of the results, irregularity of the displacement of the contact nodes and even numerical oscillations of contact reaction force may result of such discontinuity. Among the existing methods for tackling such issue, one may consider mortar elements [1, 2, 3], smoothing of the contact surfaces with additional geometrical entity (B-splines or NURBS) [4, 5, 6, 7, 8] and the use of isogeometric analysis [9, 10, 11]. In the present paper, we focus on these last two methods which are combined with a finite element code using the bi-potential method for contact management [12]. A comparative study focusing on the pros and cons of each method regarding geometrical precision and numerical stability for contact solution is proposed. The scope of this study is limited to 2D contact problems for which we consider several types of finite elements. Test cases are given in order to illustrate this comparative study.*

---

## 1 Introduction

Contact problems are inherently nonlinear since the contact area is *a priori* unknown and the associated hybrid force/displacement boundary conditions are part of the solution. The main difficulty lies in the constitutive laws of contact and friction expressed by non-smooth multivalued force-displacement relationships. In the finite element method framework, three groups of methods are usually considered for the numerical treatment of the constitutive laws of contact: (1) the penalty method [13, 6], (2) the Lagrange multiplier method [14, 15] and (3) the augmented Lagrangian method [16, 17, 18]. While the penalty method depends on a parameter that allows controlled penetrations between the structures (violation of the constraints), the Lagrange multipliers – which represent the contact reaction forces when convergence is reached – exactly enforce the non penetration conditions. However, obtaining the Lagrange multipliers requires additional operations that may lead to significantly longer computation times when a large number of contact nodes is accounted for. Augmented Lagrangian based methods advantageously combine the enforcement of non penetration conditions without considering any extra variables.

Developments presented in our study were made in the context of turbomachinery design. More precisely, the study of blade-tip/casing contacts within modern aircraft engines [19, 20] is a key element in the design of our study. Because very sensitive numerical phenomena may arise from this type of interactions such as modal interaction [21, 22, 23] or rubbing [24], contact must be managed very precisely and no penetration is acceptable. Consequently the penalty method is not eligible for our study and an augmented Lagrangian formulation combined with the bi-potential method proposed in [12] is used. In this formulation, the frictional contact problem is treated in a reduced system by means of a predictor corrector solution algorithm. In addition, the bi-potential method leads to a single displacement variational principle and a unique inequality in which unilateral contact and friction are coupled via a contact bi-potential.

Beside of being nonlinear, contact interactions are non smooth due to the discontinuity of the normal to the contact surface – namely the facetization problem – when usual finite elements are used. Nonphysical oscillations in contact forces may arise from this discontinuity and lead to chatter effect [3, 7]. The facetization of the contact surface also implies that the computation of the distance between interacting structures may be inaccurate. In order to overcome the chatter effect, three strategies are commonly given in the literature: (1) the mortar method [1, 2, 3], (2) direct smoothing of the contact surface [4, 5, 6, 7, 8], and (3) the use of isogeometric analysis [9, 10, 11]. Direct smoothing of the contact surface may advantageously imply a more accurate computation of the gap distance.

Contact interactions in aircraft engines involve large 3D industrial finite element models and any modification of the contact algorithm such as the introduction of iterative loops may lead to cumbersome computation times. As a consequence, in order to overcome the chatter effect, the choice is made to consider direct smoothing of the contact

surface. Contrary to previous study [25] focusing specifically on one smoothing strategy or an improved contact detection algorithm, the point of our work is to assess the most accurate smoothing strategy as well as the most convenient for many foreseen industrial applications by comparing two methods: (1) using a B-spline over a linear finite element mesh and (2) replacing linear finite elements by Hermite elements. The first section of this paper contains a brief recall of contact kinematics as well as the description of the contact algorithm we use. Then, the smoothing strategies are introduced and the theoretical backgrounds of B-splines and Hermite elements are detailed as well as a geometrical study in order to foresee the advantages of each smoothing strategy. Finally, both methods are compared through three contact cases allowing to assess the respect of non-penetration conditions, the quality of the algorithm when large deformations and large slidings occur and a last contact case that may be seen as a first step toward blade-tip/casing contact simulation.

## 2 Contact strategy within FEM framework

This section features a brief reminder of contact mechanics and the way it is usually handled while simulating the contact between deformable solids within the finite element method context. Also, the theoretical bases of the numerical tools we use in our comparative study are presented.

All the simulations are carried out without friction in order to focus solely on numerical sensitivity with respect to large sliding and contact detection<sup>1</sup>. While the main steps of the node-to-segment contact algorithm are recalled in this section, the reader may refer to [12] for more details regarding the contact code and the bi-potential method used for contact management.

The study is carried out within the large deformation framework – both large strains and displacements are accounted for – and all the simulations are quasi-static. A full lagrangian formulation where all the physical quantities are expressed with respect to the initial configuration is used.

### 2.1 Continuous framework

For the sake of clarity, the following theoretical developments only involve two deformable solids  $S_1$  and  $S_2$  as pictured in Fig. 1. In the initial configuration, each solid may be represented as a closed subspace of  $\mathbb{R}^2$  respectively denoted  $\overline{\Omega}_0^1$  and  $\overline{\Omega}_0^2$ . Accordingly,  $\Omega_0^\alpha$  and  $\Gamma^\alpha$  ( $\alpha = 1, 2$ , superscript  $\alpha$  will be used to refer to one of the two solids indifferently all over this section) respectively define the interior and the boundary of the closed subspace  $\overline{\Omega}_0^\alpha$  with:

$$\begin{aligned}\overline{\Omega}_0^\alpha &= \Omega_0^\alpha \cup \Gamma^\alpha \\ \Omega_0^\alpha \cap \Gamma^\alpha &= \emptyset\end{aligned}\tag{1}$$

In contact case analysis, the boundary of each body is split the following way:

$$\begin{aligned}\Gamma^\alpha &= \Gamma_u^\alpha \cup \Gamma_\sigma^\alpha \cup \Gamma_c^\alpha \\ \Gamma_u^\alpha \cap \Gamma_\sigma^\alpha &= \Gamma_\sigma^\alpha \cap \Gamma_c^\alpha = \Gamma_u^\alpha \cap \Gamma_c^\alpha = \emptyset\end{aligned}\tag{2}$$

where:

- displacements are imposed on  $\Gamma_u^\alpha$  (Dirichlet's condition)
- external forces are imposed on  $\Gamma_\sigma^\alpha$  (Neumann's condition)
- contact may occur only on  $\Gamma_c^\alpha$

The initial position of a material point  $Q$  is denoted  $\mathbf{X}^\alpha(Q)$  in the global frame and  $\mathbf{x}^\alpha(Q)$  is its final position. For each solid, an application  $\boldsymbol{\varphi}^\alpha$  is defined so that  $\mathbf{x}^\alpha(Q) = \boldsymbol{\varphi}^\alpha(\mathbf{X}^\alpha(Q))$ . Thus, the displacement of  $Q$  may be written as follows:

$$\mathbf{u}^\alpha(Q) = \mathbf{x}^\alpha(Q) - \mathbf{X}^\alpha(Q)\tag{3}$$

---

<sup>1</sup>Taking friction into account – with, for instance, the Coulomb law – for future developments, would not be an issue since it is already integrated in the contact code used in this study

For the sake of clarity, notations  $\mathbf{x}^\alpha(Q)$  and  $\mathbf{X}^\alpha(Q)$  will be respectively simplified to  $\mathbf{x}^\alpha$  and  $\mathbf{X}^\alpha$  in the following of the article.

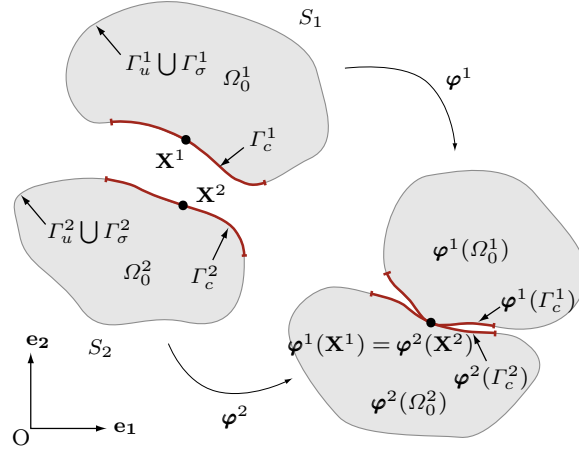


**Figure 1** – Contact problem notations.

In order to avoid any inter-penetration between the two solids, unilateral contact constraints are defined over the boundary  $\Gamma_c^\alpha$  where contact may occur. It is common to define arbitrarily a master and a slave solid for contact management. Such a definition is obviously symmetric in the continuous framework and does not have any impact on the problem formulation. In the following, superscripts <sup>1</sup> and <sup>2</sup> respectively refer to the slave and the master solids.

For any configuration, one may define the closest counterpart of a point  $\mathbf{x}^1 \in \varphi^1(\Gamma_c^1)$  – denoted  $\bar{\mathbf{x}}^2 \in \varphi^2(\Gamma_c^2)$  – as the orthogonal projection of  $\mathbf{x}^1$  onto the surface  $\varphi^2(\Gamma_c^2)$ . Which leads to the definition of both the local contact frame  $(\mathbf{t}, \mathbf{n})$  – where  $\mathbf{t}$  and  $\mathbf{n}$  respectively define the tangential and the normal direction to the contact surface – and the gap function  $g$  (Fig. 2):

$$g(\mathbf{x}^1) = \min_{\mathbf{x}^2 \in \varphi^2(\Gamma_c^2)} [(\mathbf{x}^1 - \mathbf{x}^2) \cdot \mathbf{n}] = (\mathbf{x}^1 - \bar{\mathbf{x}}^2) \cdot \mathbf{n} \quad (4)$$

Contact conditions, also known as Signorini conditions [26] may be written as:

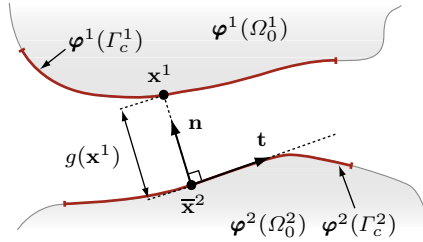


**Figure 2** – Projection of a material point.

$$g(\mathbf{x}^1) \geq 0; \quad r_n(\mathbf{x}^1) \geq 0; \quad g(\mathbf{x}^1) \cdot r_n(\mathbf{x}^1) = 0 \quad (5)$$

for any material point  $\mathbf{x}^1 \in \varphi^1(\Gamma_c^1)$  and where  $r_n(\mathbf{x}^1)$  stands for the amplitude of the contact force applied by the master solid  $S_2$  on the slave solid  $S_1$  on the material point  $\mathbf{x}^1$  and in the direction defined by the normal to  $\varphi^2(\Gamma_c^2)$  on point  $\bar{\mathbf{x}}^2$ .

Within the large deformation framework, the local form of the problem to be solved is:

$$\begin{cases} \text{DIV } \mathbf{P}(\mathbf{x}) + \mathbf{B}(\mathbf{x}) = 0 \\ \mathbf{u}(\mathbf{x}) = \bar{\mathbf{u}}(\mathbf{x}), \quad \mathbf{x} \in \varphi^\alpha(\Gamma_u^\alpha) \\ \mathbf{P}(\mathbf{x}) \cdot \mathbf{N}_0(\mathbf{x}) = \bar{\mathbf{T}}(\mathbf{x}), \quad \mathbf{x} \in \varphi^\alpha(\Gamma_\sigma^\alpha) \\ g(\mathbf{x}) \geq 0; \quad r_n(\mathbf{x}) \geq 0; \quad g(\mathbf{x}) \cdot r_n(\mathbf{x}) = 0, \quad \mathbf{x} \in \varphi^1(\Gamma_c^1) \end{cases} \quad (6)$$

where  $\mathbf{P}$  is the first Piola-Kirchhoff stress tensor,  $\mathbf{B}$  stands for the volume forces applied on the initial configuration and  $\mathbf{N}_0$  is a normal vector to  $\Gamma^\alpha$  in the initial configuration.

## 2.2 Discrete framework and solution algorithm

Several strategies have been developed in order to solve a contact problem using finite element method regarding the integration of additional contact constraints to the initial problem. In our study, the solution algorithm is based on the method proposed in [27, 28, 29] which consists in the integration of the contact forces vector to the discrete problem as an *a priori* unknown and displacement dependent force vector. The matrix form of the discrete problem is written as follows:

$$\begin{cases} \mathbf{F}_{\text{int}}(\mathbf{u}) + \mathbf{F}_{\text{ext}} + \mathbf{R}_c(\mathbf{u}) = 0 \\ \mathbf{u}(\mathbf{x}) = \bar{\mathbf{u}}(\mathbf{x}) \quad , \quad \mathbf{x} \in \boldsymbol{\varphi}^\alpha(\Gamma_u^\alpha) \end{cases} \quad (7)$$

where  $\mathbf{F}_{\text{int}}$  represents the internal forces vector,  $\mathbf{F}_{\text{ext}}$  is the external forces vector and  $\mathbf{R}_c$  is the contact forces vector that arise from the contact between solids  $S_1$  and  $S_2$ . The well-known Newton-Raphson iterative scheme is used:

$$\begin{cases} (\mathbf{K}_T)_{n+1}^i \delta \mathbf{u}_{n+1}^{i+1} = (\mathbf{F}_{\text{int}})_{n+1}^i + (\mathbf{F}_{\text{ext}})_{n+1} + \dots \\ \dots (\mathbf{R}_c(\mathbf{u}_{n+1}^{i+1}))_{n+1}^{i+1} \\ \mathbf{u}_{n+1}^{i+1} = \mathbf{u}_{n+1}^i + \delta \mathbf{u}_{n+1}^{i+1} \end{cases} \quad (8)$$

where  $\mathbf{K}_T$  is the tangent rigidity matrix,  $i$  refers to the ongoing iteration within the Newton-Raphson process and  $n$  refers to the loading increment. More details regarding the computation of matrix  $\mathbf{K}_T$  may be found in [30].

One may notice that Eq. (8) is highly nonlinear with respect to the nodal displacements vector  $\mathbf{u}$ . Indeed, the contact forces vector  $\mathbf{R}_c$  depends on  $\mathbf{u}$  which drives both the contact surface shape and the intensity of the contact reaction. Another nonlinearity may be introduced in  $\mathbf{F}_{\text{int}}$  when the considered material presents a nonlinear behaviour (hyper-elasticity, plasticity, viscoplasticity...).

Under the assumption that the tangent rigidity matrix is well-conditioned, one may invert it which yields:

$$\begin{aligned} \delta \mathbf{u}_{n+1}^{i+1} = & ((\mathbf{K}_T)_{n+1}^i)^{-1} ((\mathbf{F}_{\text{int}})_{n+1}^i + (\mathbf{F}_{\text{ext}})_{n+1}) \dots \\ & + (\mathbf{K}_T)_{n+1}^i)^{-1} (\mathbf{R}_c(\mathbf{u}_{n+1}^{i+1}))_{n+1}^{i+1} \end{aligned} \quad (9)$$

which may be written in a simpler way:

$$\begin{aligned} \delta \mathbf{u}_{n+1}^{i+1} = & (\delta \mathbf{u}_{\text{lib}})_{n+1}^{i+1} + (\delta \mathbf{u}_c)_{n+1}^{i+1} \\ \text{with:} & \\ (\delta \mathbf{u}_{\text{lib}})_{n+1}^{i+1} = & ((\mathbf{K}_T)_{n+1}^i)^{-1} ((\mathbf{F}_{\text{int}})_{n+1}^i + (\mathbf{F}_{\text{ext}})_{n+1}) \\ (\delta \mathbf{u}_c)_{n+1}^{i+1} = & (\mathbf{K}_T)_{n+1}^i)^{-1} (\mathbf{R}_c(\mathbf{u}_{n+1}^{i+1}))_{n+1}^{i+1} \end{aligned} \quad (10)$$

Thus, the displacement increment is split between a term independent from the contact problem (prediction) and a term solely depending on contact (correction). Accordingly, the general solution algorithm of a contact problem is depicted in Fig. 3.

The computation of the contact forces vector involves the results of the contact detection algorithm as well as the prediction step ( $\delta \mathbf{u}_{\text{lib}}$ ) and is carried out with the bi-potential method developed in [18, 31] and enhanced in [32, 12]. The reader may refer to those articles for extensive theoretical details about this method.

## 2.3 Detection step

This section focuses on the contact area management and the associated global detection algorithm which involves the representation of the contact surfaces  $\boldsymbol{\varphi}^\alpha(\Gamma_c^\alpha)$  from the finite element mesh. For a given contact problem, each potential contact area between both structures is defined as described in Fig. 4. Also, when the contact scenario may



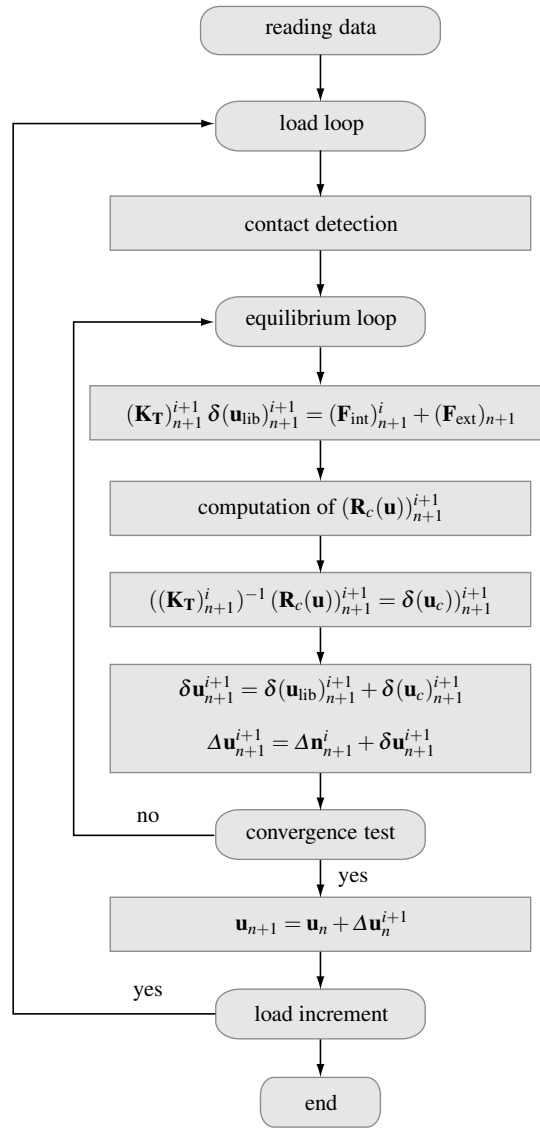


**Figure 3** – General solution algorithm.

be anticipated, this formalism advantageously allows for optimizing computation times through the minimization of the number of nodes taken into account for the contact detection step thus minimizing the dimension of the problem to solve in order to obtain the contact forces vector  $\mathbf{R}_c$ . Indeed, the bi-potential method implies a condensation step in which  $\mathbf{R}_c$  is obtained thanks to a system reduced to the active contact nodes.

At the beginning of a load step, for each contact area, the detection algorithm computes the minimal distance between each node belonging to the contact surface of the slave solid and the contact the surface of the master solid. If this distance is superior to the alert distance  $d_a$  then the node is not considered for the solution of the contact problem thus optimizing computation times.

The orthogonal projection of a potential contact node  $\mathbf{x}_k^1$  in the contact areas of the master solid is depicted in Fig. 5 for the spatially discretized problem. This projection – made once the closest target segment on  $S_2$  has been identified – is a key feature of the *contact detection* step of the algorithm described in Fig. 3 since it determines all the required quantities for a considered contact node. These quantities are detailed in Fig. 6.

Using the notations given in Fig. 5, and when a linear finite element mesh is considered for the master solid, the

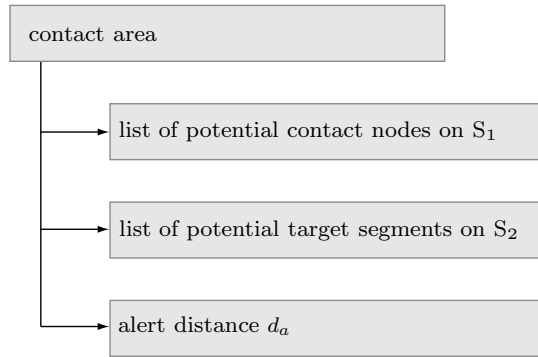


**Figure 4** – Definition of a contact area.

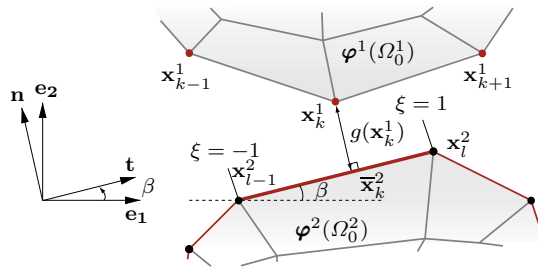


**Figure 5** – Orthogonal projection of a contact node.

projection simply consists in obtaining the equation of the line perpendicular to the segment  $[x_{l-1}^2, x_l^2]$  passing by  $x_k^1$ . When smoothing procedures are considered, the projection of a contact node onto the contact surface of the master solid requires iterative procedures detailed in the following.

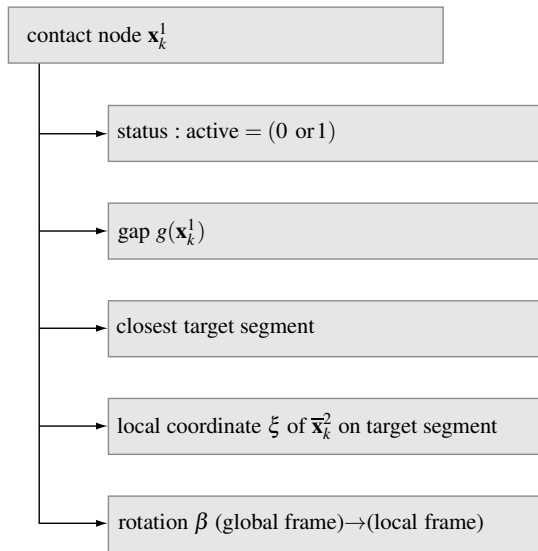


**Figure 6** – Definition of a contact node.

### 3 Smoothing strategies dedicated to the representation of contact surfaces

This section focuses on the two distinct strategies considered in our study in order to avoid the facetization phenomenon of the master contact surface. The first method features an additional geometric entity made of B-spline patches superimposed to the finite element mesh while the second method is based on Hermite finite elements which contain additional degrees of freedom on each node in order to ensure the continuity of the tangent to an edge at the junction between two elements. Finally, the improvements in terms of the representation of a curved surface resulting from the use of these two methods are detailed.

#### 3.1 Splines

Among the available mathematical objects used for smoothing, the Bézier and B-spline curves are the most popular forms to date. At each time step, these curves are computed from the position of each node of the contact surface and are then used to determine the gap between structures as well as the direction of the normal to the contact surface. While preserving the original meshes, these curves remove the facetization issues, ease the contact transition and then increase the convergence rates of the dedicated contact algorithms.

Several methods are available for the direct smoothing of a contact surface based on parametric curves among which Non Uniform Rational B-splines (NURBS) [10, 11] and Overhauser splines [33, 34] to name a few. NURBS are very popular, their main advantage lies in the fact they can perfectly reproduce a circular profile while other spline functions can only closely approximate it [35]. Accordingly, NURBS are frequently used when rigid circular profiles are considered. When large deformations arise or that both contacting bodies are flexible, uniform splines such as cubic B-splines may be of great interest since their simpler description may significantly reduce computation times [19].

In the present study, the cubic B-spline approach is adopted since it can easily be adapted to finite element meshes where the current positions of the nodes only are required. This section is intended to give the reader the basic mathematical tools to understand the construction of B-splines curves.

#### Mathematical definition

Given an interval  $[a, b] \in \mathbb{R}$ , and  $\Omega_{\text{npt}} = (t_i)_{i=0, \text{npt}}$  a partition – called knot sequence – of this interval such as  $t_0 = a$ ,  $t_{\text{npt}} = b$  and  $t_0 < \dots < t_{\text{npt}}$ . The function  $s : [a, b] \rightarrow \mathbb{R}$  is a polynomial spline function of degree  $n$  if:

$$\begin{aligned} (i) \quad & s \in C^{n-1}([a, b]) \\ (ii) \quad & \forall i \in [0..npt - 1], \forall t \in [t_i, t_{i+1}], s \in \mathcal{P}_n \end{aligned} \quad (11)$$

where  $\mathcal{P}_n$  is the space of polynomial functions of degree equal or inferior to  $n$ . The space of polynomial spline functions of degree  $n$  and defined over  $\Omega_{\text{npt}}$  is denoted  $S_n(\Omega_{\text{npt}})$ , it is a vectorial space of dimension  $npt + n$ .

Among all the eligible bases of  $S_n(\Omega_{\text{npt}})$ , we focus on the one constituted by the B-splines<sup>2</sup> of degree  $n$ . A polynomial spline function  $s \in S_n(\Omega_{\text{npt}})$  is a B-spline if:

$$\begin{aligned} \exists i \in [0..npt - n - 1], \forall t \in [a, b] \\ \bullet \quad & s(t) = 0, \forall t \in [t_0, t_{\text{npt}}] \setminus [t_i, t_{i+n+1}] \\ \bullet \quad & \forall t \in [t_i, t_{i+n+1}], s(t) \geq 0 \end{aligned} \quad (12)$$

Consequently a B-spline, associated with a point  $t_i$ , is denoted  $B_{ni}(t)$ .

#### Uniform B-spline curves

B-spline bases [36] allow for the construction of complex parametric spatial curves  $\mathbf{c}(t)$ <sup>3</sup> by multiplying a spline basis functions  $B_{ni}(t)$  and a set of control points  $\mathbf{Q}_i$ <sup>4</sup>:

$$\mathbf{c}(t) = \sum_{i=0}^{N-1} \mathbf{Q}_i B_{ni}(t) \quad (13)$$

<sup>2</sup>B-splines stands for basic splines.

<sup>3</sup>In a three-dimensional cartesian space, the parametric curve is a vector-valued function of parameter  $t$  such as  $\mathbf{c}(t) = [c_x(t), c_y(t), c_z(t)]$ .

<sup>4</sup>In a three-dimensional cartesian space, the control points are stored along the three directions such as  $\mathbf{Q}_i = [Q_{xi}, Q_{yi}, Q_{zi}]$

They result by mapping a dimension  $t$  defined along a knot sequence  $(t_i)_{i=0,npt}$  into a Cartesian space through control points and are completely specified by the curve's control points, the curve's polynomial degree and the B-spline basis functions as detailed in equation (13).

The B-spline considered will be characterized by its degree  $n$  and the knot sequence defined here by the following considerations:

- Choosing  $n = 3$  provides a  $C^1$  continuity to the normal of the contact surface, which is of primary importance to correctly calculate the distance between the structures and to avoid numerical jumps in the estimation of the contact forces. Lower degree polynomials do not provide sufficient control of the surface's shape and higher degree polynomials are computationally more expensive.
- The knot sequence can be either uniform or nonuniform. A curve is uniform if the spacing between all the knots is constant  $t_{i+1} = t_i + 1$ .

Consequently, *cubic uniform* B-spline curves are used in this research. Each segment  $p$  of the curve<sup>5</sup> can be then written in a matrix form:

$$c_p(t) = \mathbf{T}\mathbf{M}\mathbf{Q}_p \quad (14)$$

where  $\mathbf{T} = (t^3, t^2, t, 1)$ ,  $\mathbf{Q}_p^t = (Q_{p-1}, Q_p, Q_{p+1}, Q_{p+2})$  and:

$$\mathbf{M} = \frac{1}{6} \begin{bmatrix} -1 & 3 & -3 & 1 \\ 3 & -6 & 3 & 0 \\ -3 & 0 & 3 & 0 \\ 1 & 4 & 1 & 0 \end{bmatrix} \quad (15)$$

### Interpolation

By construction, a B-spline does not pass through its control points  $\mathbf{Q}$ . Nevertheless, a better control of the spline is achieved when the latter interpolates the control points. This way, the condition to match the original geometry of the contact line is satisfied. The inversion method addresses this issue by finding the  $N + 2$  control points  $Q_i$ , given a set of  $N$  data points  $P_i$  to be interpolated.  $N$  linear equations are generated based on the fact that  $c(t)$  has to pass through the data points.

In the case of a uniform parametrization, segment  $p$  of the spline curve reaches its extremal points  $P_p$  and  $P_{p+1}$  for extremal values of parameter  $t$ , respectively  $t = 0$  and  $t = 1$ . Accordingly, it yields for  $p = 0, \dots, N - 2$ :

$$\begin{aligned} P_p &= c_p(0) = \frac{1}{6}(Q_{p-1} + 4Q_p + Q_{p+1}) \\ P_{p+1} &= c_p(1) = \frac{1}{6}(Q_p + 4Q_{p+1} + Q_{p+2}) \end{aligned} \quad (16)$$

where  $c_p(1) = c_{p+1}(0)$ . System (16) can be recast in a matrix form such as:

$$\begin{pmatrix} \text{end 1} \\ P_0 \\ P_1 \\ \vdots \\ P_{N-2} \\ P_{N-1} \\ \text{end 2} \end{pmatrix} = \frac{1}{6} \begin{bmatrix} \text{e n d c o n d i t i o n s 1} \\ 1 & 4 & 1 & 0 & \dots & 0 \\ 0 & 1 & 4 & 1 & 0 & \dots & 0 \\ \vdots & & & \ddots & & & \vdots \\ 0 & \dots & 0 & 1 & 4 & 1 & 0 \\ 0 & & \dots & 0 & 1 & 4 & 1 \\ \text{e n d c o n d i t i o n s 2} \end{bmatrix} \begin{pmatrix} Q_{-1} \\ Q_0 \\ Q_1 \\ \vdots \\ Q_{N-2} \\ Q_{N-1} \\ Q_N \end{pmatrix}$$

or, in a contracted way:

$$\mathbf{P} = \mathbf{A}\mathbf{Q} \quad (17)$$

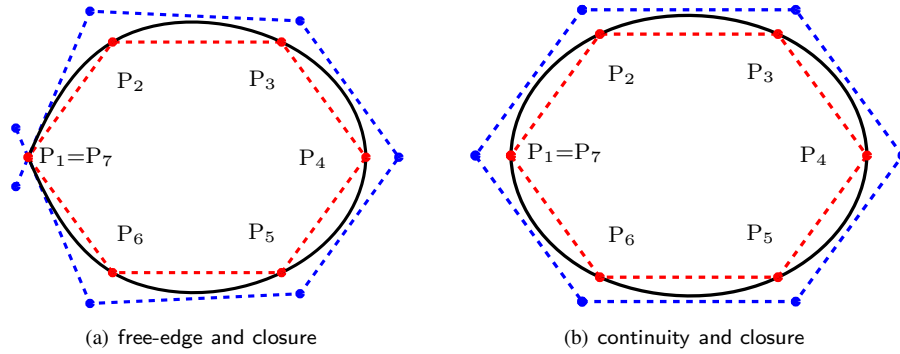


**Figure 7** – two types of end condition: spline (—), data points  $\mathbf{P}$  (●) and control points  $\mathbf{Q}$  (●)

where the two end-conditions required to uniquely solve the problem have to be specified.

### End conditions

Various methods are available for the definition of the boundary or end-conditions of an interpolating spline curve. Two different types of end-condition are investigated: (1) free edges and continuity and (2) closure conditions in case the contact line is not open. The first one is dealt with the double vertex approach [37]:

$$Q_{-1} = Q_0 \quad \text{and} \quad Q_N = Q_{N-1} \quad (18)$$

which assumes that the curvature of the spline curve at each end is zero. The second one requires the position of the spline  $c(t)$ , its first  $c(t)'$  and second  $c(t)''$  spatial derivatives to be equal at the end tips, mathematically leading to:

$$\begin{aligned} c_0(0) = c_{N-2}(1) &\Leftrightarrow P_0 = P_{N-1} \\ c'_0(0) = c'_{N-2}(1) &\Leftrightarrow -Q_{-1} + Q_1 = -Q_{N-2} + Q_N \\ c''_0(0) = c''_{N-2}(1) &\Leftrightarrow Q_{-1} - 2Q_0 + Q_1 = Q_{N-2} - \dots \\ &\dots 2Q_{N-1} + Q_N \end{aligned} \quad (19)$$

### Detection procedure

The closest counterpart of a contact node on a spline is identified in two steps:

1. a quick distance test between the contact node and each node of the contact surface allows to identify the two closest elements to the contact node.
2. over each of these two elements a Newton-Raphson iterative algorithm [38] yields the local coordinate  $\xi$  of the closest counterpart to the contact node. The valid counterpart is the one satisfying  $\xi \in [-1; 1]$ .

## 3.2 Hermite elements

### Definition

In order to avoid the construction of an additional mathematical tool such as a B-spline for the smoothing of linear finite elements, other strategies focus on the use of more specific finite elements which, by construction, impose the continuity of the direction of the normal vector to the contact surface. By definition,  $C^0$  elements only ensure the continuity of their embedded degrees of freedom – the displacements of the nodes – between two consecutive elements. Consequently, one may think of adding degrees of freedom associated with the tangent vector to the edge of the element. In our case, additional informations required are linked with the spatial derivatives of the displacements

<sup>5</sup>As already mentioned, a curve is generally vector-valued but is written here along a single direction of the Cartesian space for the sake of simplicity.

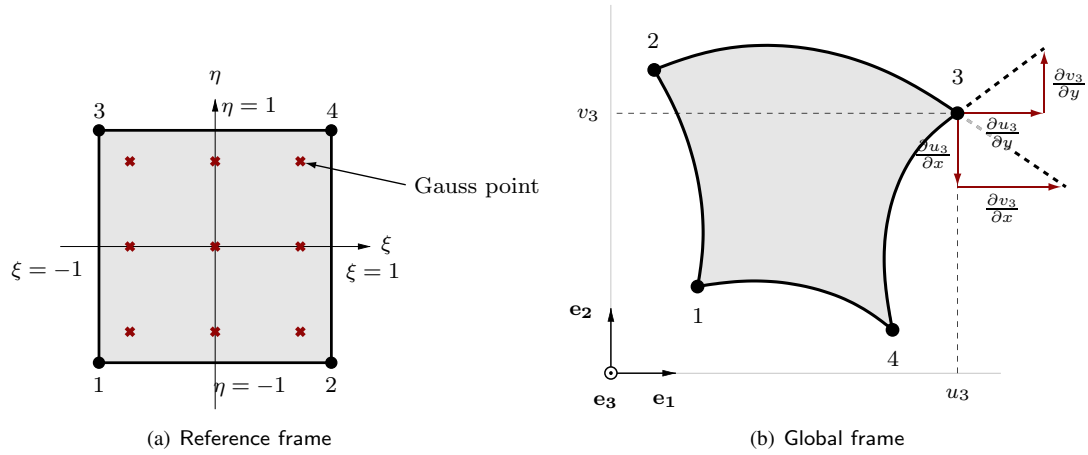


**Figure 8** – Illustration of Hermite element construction

of each node in each direction. Considering two-dimensional elements, four extra degrees of freedom are thus required per node. Accordingly, an usual 4-node two-dimensional elements increases its number of degrees of freedom from 8 to 24 (figure 8) :

$$\mathbf{u}(\xi, \eta) = \mathbf{N}(\xi, \eta) \mathbf{u}^e = \mathbf{N}(\xi, \eta) (\mathbf{u}_1, \mathbf{u}_2, \mathbf{u}_3, \mathbf{u}_4)^T \quad (20)$$

where:

$$\mathbf{u}_i = \left\{ u_i, \frac{\partial u_i}{\partial x}, \frac{\partial u_i}{\partial y}, v_i, \frac{\partial v_i}{\partial x}, \frac{\partial v_i}{\partial y} \right\} \quad (21)$$

and  $i = (1, 2, 3, 4)$  is the node number. The counterpart of the increased number of degrees of freedom per node is the modification of the order of the shape functions which may allow for a less dense mesh with a smaller number of elements. The choice is made to consider an isoparametric element with cubic functions belonging to the following polynomial basis:

$$\langle P \rangle = \langle 1 \quad \xi \quad \eta \quad \xi^2 \quad \xi\eta \quad \eta^2 \quad \xi^3 \quad \xi^2\eta \quad \xi\eta^2 \quad \eta^3 \dots \dots \xi^3\eta \quad \xi\eta^3 \rangle \quad (22)$$

which leads to the subsequent shape functions:

$$\begin{aligned} N_1(\xi, \eta) &= 0.125(1-\xi)(1-\eta)(2-\xi^2-\eta^2-\xi-\eta) \\ N_2(\xi, \eta) &= 0.125(1-\xi)(1-\eta)(1-\xi^2) \\ N_3(\xi, \eta) &= 0.125(1-\xi)(1-\eta)(1-\eta^2) \\ N_4(\xi, \eta) &= 0.125(1+\xi)(1-\eta)(2-\xi^2-\eta^2+\xi-\eta) \\ N_5(\xi, \eta) &= -0.125(1+\xi)(1-\eta)(1-\xi^2) \\ N_6(\xi, \eta) &= 0.125(1+\xi)(1-\eta)(1-\eta^2) \\ N_7(\xi, \eta) &= 0.125(1+\xi)(1+\eta)(2-\xi^2-\eta^2+\xi+\eta) \\ N_8(\xi, \eta) &= -0.125(1+\xi)(1+\eta)(1-\xi^2) \\ N_9(\xi, \eta) &= -0.125(1+\xi)(1+\eta)(1-\eta^2) \\ N_{10}(\xi, \eta) &= 0.125(1-\xi)(1+\eta)(2-\xi^2-\eta^2-\xi+\eta) \\ N_{11}(\xi, \eta) &= 0.125(1-\xi)(1+\eta)(1-\xi^2) \\ N_{12}(\xi, \eta) &= -0.125(1-\xi)(1+\eta)(1-\eta^2) \end{aligned} \quad (23)$$

Derivatives of the shape functions with respect to the variable  $\xi$  are:

$$\begin{aligned}
N_1(\xi, \eta)_{,\xi} &= 0.125(1 - \eta)(-3 + 3\xi^2 + \eta^2 + \eta) \\
N_2(\xi, \eta)_{,\xi} &= -0.125(1 - \xi)(1 - \eta)(1 + 3\xi) \\
N_3(\xi, \eta)_{,\xi} &= 0.125(-1 + \eta)(1 - \eta^2) \\
N_4(\xi, \eta)_{,\xi} &= 0.125(1 - \eta)(3 - 3\xi^2 - \eta^2 - \eta) \\
N_5(\xi, \eta)_{,\xi} &= -0.125(1 + \xi)(1 - \eta)(1 - 3\xi) \\
N_6(\xi, \eta)_{,\xi} &= 0.125(1 - \eta)(1 - \eta^2) \\
N_7(\xi, \eta)_{,\xi} &= 0.125(1 + \eta)(3 - 3\xi^2 - \eta^2 + \eta) \\
N_8(\xi, \eta)_{,\xi} &= -0.125(1 - \xi)(1 + \eta)(1 - 3\xi) \\
N_9(\xi, \eta)_{,\xi} &= -0.125(1 + \eta)(1 - \eta^2) \\
N_{10}(\xi, \eta)_{,\xi} &= 0.125(1 + \eta)(-3 + 3\xi^2 + \eta^2 - \eta) \\
N_{11}(\xi, \eta)_{,\xi} &= 0.125(1 - \xi)(1 + \eta)(1 + 3\xi) \\
N_{12}(\xi, \eta)_{,\xi} &= 0.125(1 + \eta)(1 - \eta^2)
\end{aligned} \tag{24}$$

Derivatives of the shape functions with respect to the variable  $\eta$  are:

$$\begin{aligned}
N_1(\xi, \eta)_{,\eta} &= 0.125(1 - \xi)(-3 + \xi^2 + 3\eta^2 + \xi) \\
N_2(\xi, \eta)_{,\eta} &= 0.125(-1 + \xi)(1 - \xi^2) \\
N_3(\xi, \eta)_{,\eta} &= -0.125(1 - \xi)(1 - \eta)(1 + 3\eta) \\
N_4(\xi, \eta)_{,\eta} &= 0.125(1 + \xi)(-3 + \xi^2 + 3\eta^2 - \xi) \\
N_5(\xi, \eta)_{,\eta} &= 0.125(1 + \xi)(1 - \xi^2) \\
N_6(\xi, \eta)_{,\eta} &= -0.125(1 + \xi)(1 - \eta)(1 + 3\eta) \\
N_7(\xi, \eta)_{,\eta} &= 0.125(1 + \xi)(3 - \xi^2 - 3\eta^2 + \xi) \\
N_8(\xi, \eta)_{,\eta} &= 0.125(-1 - \xi)(1 - \xi^2) \\
N_9(\xi, \eta)_{,\eta} &= -0.125(1 + \xi)(1 + \eta)(1 - 3\eta) \\
N_{10}(\xi, \eta)_{,\eta} &= 0.125(1 - \xi)(3 - \xi^2 - 3\eta^2 - \xi) \\
N_{11}(\xi, \eta)_{,\eta} &= 0.125(1 - \xi)(1 - \xi^2) \\
N_{12}(\xi, \eta)_{,\eta} &= -0.125(1 - \xi)(1 + \eta)(1 - 3\eta)
\end{aligned} \tag{25}$$

The shape functions and their derivatives are defined with respect to nodal variables over the reference element and numerical integration required for the computation of elementary matrices is made using Gauss-Legendre formulae with nine integration points pictured as a cross in Fig. 8.

Regarding the detection procedure used for the determination of the closest counterpart of a contact node on the contact surface – as described in Fig. 6 – it is first necessary to identify the closest element. Over the curve edge of this element, the closest counterpart of the contact node minimizes the gap function  $g(\mathbf{x}^1)$ . For  $\eta = 1$ , the closest counterpart is given by the solution of the minimization problem:

$$\bar{\xi} = \arg \min_{\xi \in [-1, 1]} \|\mathbf{x}^1 - \mathbf{N}(\xi, 1)\mathbf{u}^e\| \tag{26}$$

This problem is solved thanks to a typical Newton-Raphson algorithm.

During the detection step of the contact algorithm, one must determine the rotation angle  $\beta$  between the local contact frame and the fix global frame. This angle may be easily computed considering the definition of the additional dof contained in the Hermite element. Depending on the edge which is considered in the element, the pair  $(\frac{\partial u_i}{\partial x}, \frac{\partial u_i}{\partial y})$  or

$(\frac{\partial v_i}{\partial x}, \frac{\partial v_i}{\partial y})$  defines the tangent vector  $\mathbf{t}$  to the edge on the node of interest. Thus, the normal  $\mathbf{n}$  and the angle  $\beta$  may be defined as:

$$\mathbf{n} = \mathbf{e}_3 \wedge \mathbf{t} \quad (27)$$

and:

$$\beta = \arctan\left(\frac{\mathbf{n} \cdot \mathbf{e}_2}{\mathbf{n} \cdot \mathbf{e}_1}\right) \quad (28)$$

Hermite elements also require specific attention during the meshing procedure. Indeed, these elements can only be used under the condition that a parametric formulation of the surface to discretize is known. For the sake of brevity, this aspect is not detailed in this paper. In our study, test cases are based on relatively simple geometries that allow for easy parametrization of the surfaces.

### Static behaviour

The contact algorithm considered in our study allows for the computation of the contact reaction force generated by the master surface over the node of the slave structure as a nodal force denoted  $r_n(\mathbf{x}^1)$  in Eq. (5). The principle of action and reaction requires this force to be also applied on the master surface. Since the contact solution algorithm is based on a node-to-segment approach, the equivalent nodal forces applied on each node of the targeted element of the master surface are obtained from the local coordinate  $\xi$  determined during the detection step (as detailed in Fig. 6). If a punctual force  $\mathbf{F} = F_x \mathbf{e}_1 + F_y \mathbf{e}_2$  is applied on the edge of a finite element, the nodal components of this force are:

$$\mathbf{F}^e = \mathbf{N}^T(\xi, \eta) \{F_x, F_y\} \quad (29)$$

where

$$\mathbf{N} = \begin{bmatrix} N_1 & N_2 & N_3 & 0 & 0 & 0 & \cdots & 0 & 0 & 0 \\ 0 & 0 & 0 & N_1 & N_2 & N_3 & \cdots & N_{10} & N_{11} & N_{12} \end{bmatrix} \quad (30)$$

Using Hermite elements for a contact simulation requires a good understanding of their specific mechanical behaviour. Indeed, the application of a punctual force at a given position along one edge of the element leads to a non typical response because of its shape functions. The comparison of the solution obtained with  $Q4$ ,  $Q8$  (respectively linear four-noded and quadratic eight-noded finite elements) and Hermite elements when a force is applied in the middle of the top edge ( $\eta = 1$  et  $\xi = 0$ ) of each finite element – as pictured in Figs. 9, 10 and 11 – underlines this specificity. In each case, three consecutive elements are considered in order to highlight potential irregularities along the top edges between two elements and all the degrees of freedom associated with the lower nodes are clamped.

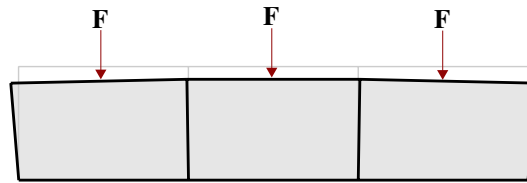


**Figure 9** – Punctual forces applied on  $Q4$  elements

Obviously, due to an enriched formulation,  $Q8$  and Hermite elements feature a more complex behaviour than  $Q4$  elements. Also, it is noticeable that Hermite elements are the only ones allowing for the continuity of the normal to the upper edge from an element to another. To the contrary, dashed lines in Fig. 10 highlight the discontinuity of this normal for  $Q8$  elements. In this particular case,  $Q8$  elements lead to a more severe slope discontinuity than  $Q4$  elements, that is the reason why  $Q8$  (and  $Q12$ ) elements are not considered for the study of contact problems. Following contact simulations are made in the light of these results which will matter for their interpretation.



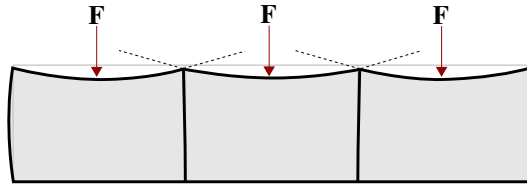


**Figure 10** – Punctual forces applied on  $Q8$  elements

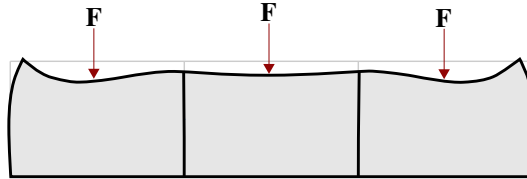


**Figure 11** – Punctual forces applied on Hermite elements

### 3.3 Geometrical considerations

As mentioned previously, smoothing strategies allow for both a more precise computation of the gap or penetrations between structures as well as the elimination of the discontinuity of the direction of the normal to the contact surface which is a numerical improvement.

This section intends to highlight the geometrical improvements – the more precise computation of the gap and the orientation of the normal to the contact surface – from the use of smoothing methods on a simple test case.

#### Discretization errors

In order to assess the quality of the discretization of each method, the focus is made on a half-ring – pictured in Fig. 12 – meshed with one layer of finite elements over its width and  $n_e$  elements over its circumference. Two parameters are considered: (1) the gap error  $g$ , which represents the gap between the contact surface and the actual perfect half-circle that should be the external line of the half-ring, and (2) the normal orientation error  $\delta\theta$  that stands for difference between the direction of the normal vector  $\vec{n}$  to the surface for a given discretization method with the direction of the normal vector  $\vec{n}_t$  to the perfect circle. A representation of these two parameters is given in Fig. 12. Nodes on the two extremities of the half ring are clamped.

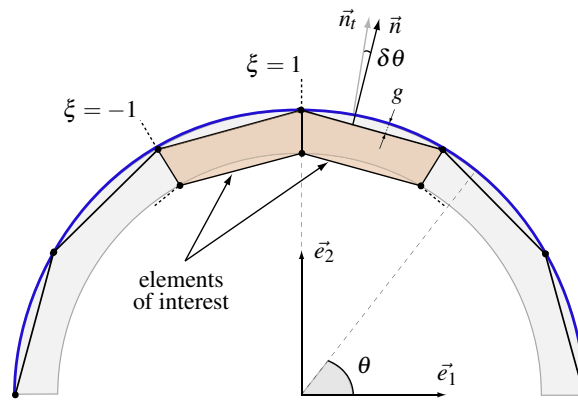


**Figure 12** – Test case for assessment of the geometrical improvement.

In total, five types of discretization are considered for the half-ring:

- linear four-noded finite elements ( $Q4$ );
- quadratic eight-noded finite elements ( $Q8$ );

- cubic twelve-noded finite elements ( $Q_{12}$ );
- $Q_4$  elements with B-spline interpolation<sup>6</sup>;
- Hermite elements

For each case, only even numbers ( $n_e = 16, 18, 20, 22, 24, 26, 28$  and  $30$ ) of elements along the circumference of the half-ring are taken into account and our study focuses on the two elements around  $\theta = \frac{\pi}{2}$  highlighted in Fig. 12.

## Gap error

The gap error  $g$  (in percent of the external radius of the ring) is pictured in Fig. 13 for each discretization method and for different mesh parameters. Each curve corresponds to one of the eight values considered for  $n_e$  (the darker the line, the higher  $n_e$ ). The evolution of the error is represented with respect to the local coordinate  $\xi$  varying from -1 to 1 while describing the upper edge ( $\eta = 1$ ) of each of the two finite elements of interest around the position  $\theta = \frac{\pi}{2}$  as shown in Fig. 12.

As expected, for each discretization method, the gap error decreases when the mesh parameter  $n_e$  increases. All the figures have the same scale – to the exception of the case involving linear elements since the results order of magnitude is not comparable – so that one may easily compare the quality of each method. It appears that the cubic twelve-noded elements give the best results: the gap error remains between  $-1 \cdot 10^{-4} \%$  and  $+5 \cdot 10^{-5} \%$  throughout the two edges. To the contrary, linear finite elements lead to the largest gap error with a maximum of  $0.13 \%$  with 30 finite elements along the circumference of the half ring.

The two smoothing methods lead to similar results and the maximum error is comparable to the one obtained with quadratic elements. Overall, results obtained with linear, quadratic and cubic finite elements may be comparable with those obtained with smoothing methods in terms of maximum error but it is noticeable that they feature a non-continuous slope for  $\theta = \frac{\pi}{2}$  which appears even more obviously when looking at the normal orientation error.

## Normal orientation error

One of the main weaknesses of a typical finite element discretization is the well known *facetization* phenomenon leading to the discontinuity of the orientation of the normal vector to the contact surface. More precisely, in the case of linear elements, the orientation of the normal vector is piece wise linear while the spline and Hermite discretizations allow for it to be  $C^1$ -continuous. When quadratic or cubic elements are involved, results may be enhanced but the discontinuity remains.

The errors on the orientation  $\delta\theta$  of the normal to the contact surface are pictured in Fig. 14. Same as for the gap error, the differences between the contact orientation obtained with the discretization methods and the perfect geometric definition of the ring decrease while the mesh parameter  $n_e$  increases.

To the contrary of what was observed in terms of gap error, results obtained with the cubic twelve-noded elements are relatively close to those obtained with the two smoothing methods, thus highlighting their accuracy. In addition, the two smoothing methods advantageously feature the continuity of the normal vector to the contact surface that is highlighted by the continuity of the normal orientation error for  $\theta = \frac{\pi}{2}$ . The discontinuity observed for linear, quadratic and cubic elements is the base of the facetization phenomenon.

## Conclusion

Results obtained for the simple test case depicted in Fig. 12 underline that the fundamental issue of the discontinuity of the normal to the contact surface while moving from an element to its neighbour exists with usual finite elements, no matter their degree. When smoothing procedures are considered, this issue disappears and the precision over the gap computation is increased in comparison to linear and even quadratic finite elements. Only cubic elements may provide a better accuracy in terms of gap computation but their use comes at a cost of a significant increase of the computation

---

<sup>6</sup>"B-spline interpolation" simply refers to the interpolation of the nodes on the contact surface by the B-spline.

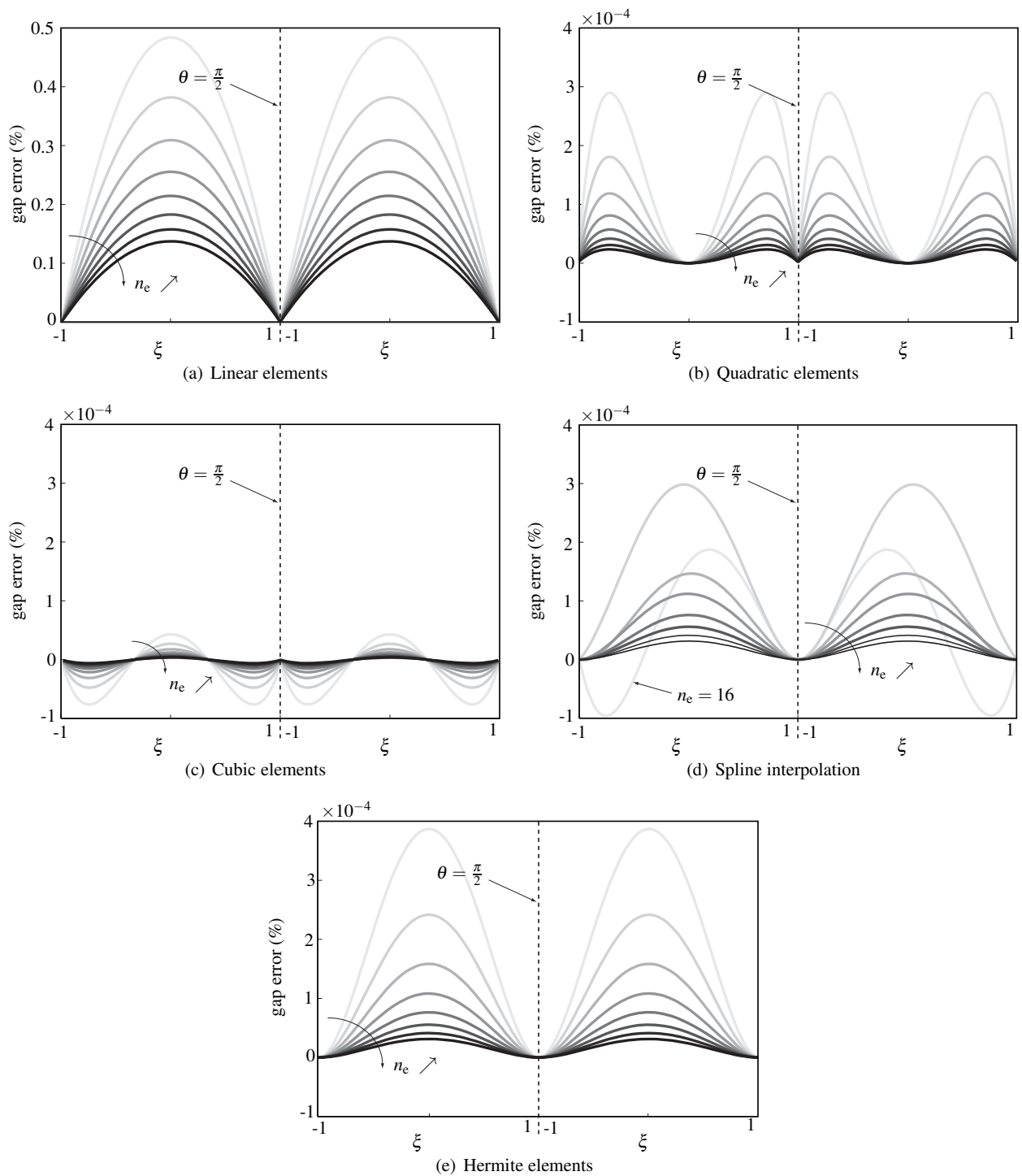


**Figure 13** – Gap error  $g$  for  $n_e = 16, 18, 20, 22, 24, 26, 28$  and  $30$  ( $\theta = \frac{\pi}{2}$  refers to Fig. 12).

times due to a much larger number of degrees of freedom. Accordingly, this geometrical study suggests that the two smoothing methods offer a nice compromise between results accuracy and computation times. As such, they seem well-suited for the study of contact problems with large slidings.

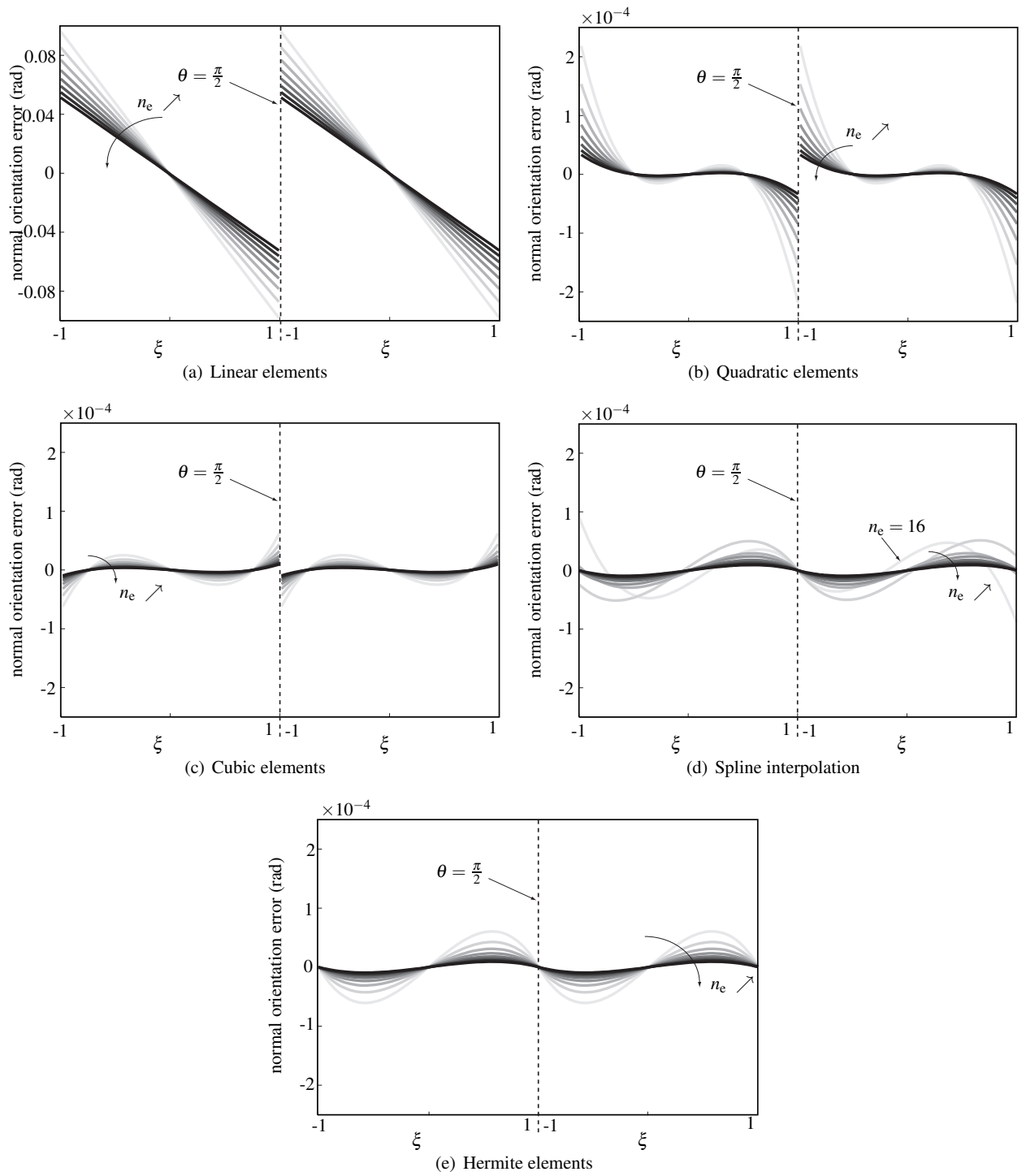


**Figure 14** – Normal orientation error  $\delta\theta$  for  $n_e = 16, 18, 20, 22, 24, 26, 28$  and  $30$  ( $\theta = \frac{\pi}{2}$  refers to Fig. 12).

The interpolation of the contact surface with a B-spline usually goes along with linear finite elements<sup>7</sup> in order

<sup>7</sup>Eventhough any type of finite element - such as quadratic, cubic or enriched - could be used, results provided in section 3.3 hint that using a B-spline interpolation over richer elements such as quadratic elements would lead to an unnecessary increase of computation times.

to minimize computation times[34, 39]. Accordingly, in order to proceed to a relevant comparison of the contact simulations and to assess the improvements due to the use of a B-spline, only finite elements  $Q4$  are considered in the following in addition to the two smoothing methods.

## 4 Comparative study under large sliding

This section focuses on assessing the enhancement of the solution of finite element computations when the smoothing strategies aforementioned (B-splines and Hermite elements) are used. For each contact case, simulations are carried out three times:

1. with  $Q4$  elements and no smoothing of the contact surface,
2. with  $Q4$  elements and B-spline smoothing of the contact surface,
3. with Hermite elements.

### 4.1 case 1: beam and half-ring

The first contact case aims at validating the contact detection procedure. Two structures are considered: a half-ring clamped on its extremities and a beam clamped on its right extremity as pictured in Fig. 15. The Young's moduli are respectively  $E_r = 10^6$  Pa and  $E_b = 90 \cdot 10^6$  Pa for the ring and the beam. A load  $\vec{F} = -\|F\|\vec{y}$  is imposed on the left extremity of the beam ( $\|F\| = 50$  kN). The contact zone is defined between the upper edge of the half-ring (master surface) and the lower edge of the beam (slave surface).

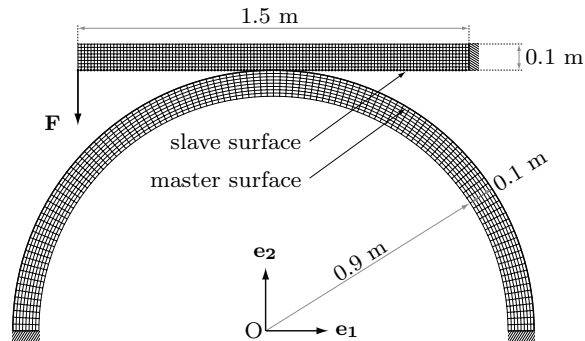


**Figure 15** – Contact configuration of case 1.

### Mesh definition

A convergence study is carried out to define the number of layers of elements for each structure in order to have an accurate representation of bending and static simulations are launched for both structures with variation of the number of elements over the width and over the length (or circumference for the half-ring) of both structures. These simulations are carried out independently for each structure without contact. Consequently, results displayed in Tab. 1 may not be compared with any result obtained for contact simulations presented in the next sections.

Results show that for each structure, at least 100 elements on the length and 8 elements on the width are required to get accurate results. In addition to the mesh convergence, it is chosen to impose that the gap error – defined in section 3.3 – for linear discretization should be less than 0.01 % which is satisfied when considering at least 120 elements over the circumference of the half-ring. Parameters  $\eta = 120$  and  $\mu = 8$  are chosen for the numerical simulations carried out in the following. These values allow for both an accurate representation of the contact surface and the bending of the structures of interest. These mesh parameters are also used when Hermite elements are considered.

mesh parameters	Q4	H4
$\eta = 30. \mu = 2$	0.259	0.287
$\eta = 60. \mu = 4$	0.282	0.284
$\eta = 120. \mu = 8$	0.288	0.290
$\eta = 240. \mu = 16$	0.290	0.290

**Table 1** – Norm of the maximum displacement for the beam with different mesh parameters ( $\eta$  number of elements over the length/circumference and  $\mu$  number of elements over the width).

### Detection procedure

In order to validate the detection procedure, the half-ring is first considered perfectly rigid. As a consequence, the contact nodes of the flexible beam embrace the circular profile of the half-ring as depicted in Fig. 16 with B-splines. No penetration or irregularity is observed thus validating the detection algorithm. Identical results are obtained with Hermite elements

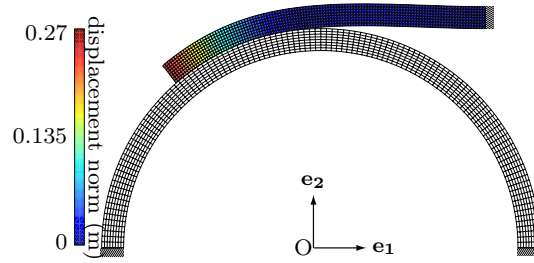


**Figure 16** – Deformed structures after loading the beam with B-splines interpolation over a rigid ring (identical results are obtained with Hermite elements).

When the half-ring is flexible, its deformation leads to a significant relative sliding between the two contact surfaces. As a result, the numerical resolution of this contact case is much more challenging. At the end of the simulation, both the beam and the half-ring are largely deformed as depicted in Fig 17. No difference could be seen between simulations carried out with B-splines and Hermite elements: displacements of both structures perfectly match.

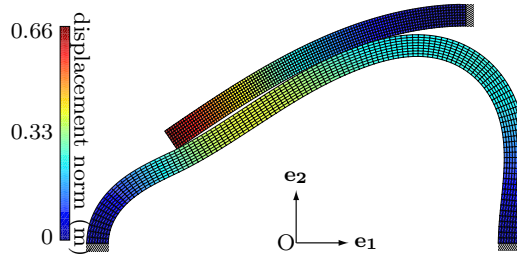


**Figure 17** – Deformed structures after loading the beam with Hermite elements (identical results are obtained with B-splines).

The results obtained with this first contact case highlight the quality of the detection algorithm with the two smoothing strategies of interest. Logically, these two strategies are now applied to more complex contact cases involving large slidings and for which the limits associated with the use of a usual linear mesh should appear clearly.

## 4.2 case 2: square and half-rings

The second test case intends to validate contact detection when large slidings occur between the contacting structures. Two half-rings and a square are considered as depicted in Fig. 18(a). Both half-rings are clamped on their extremities

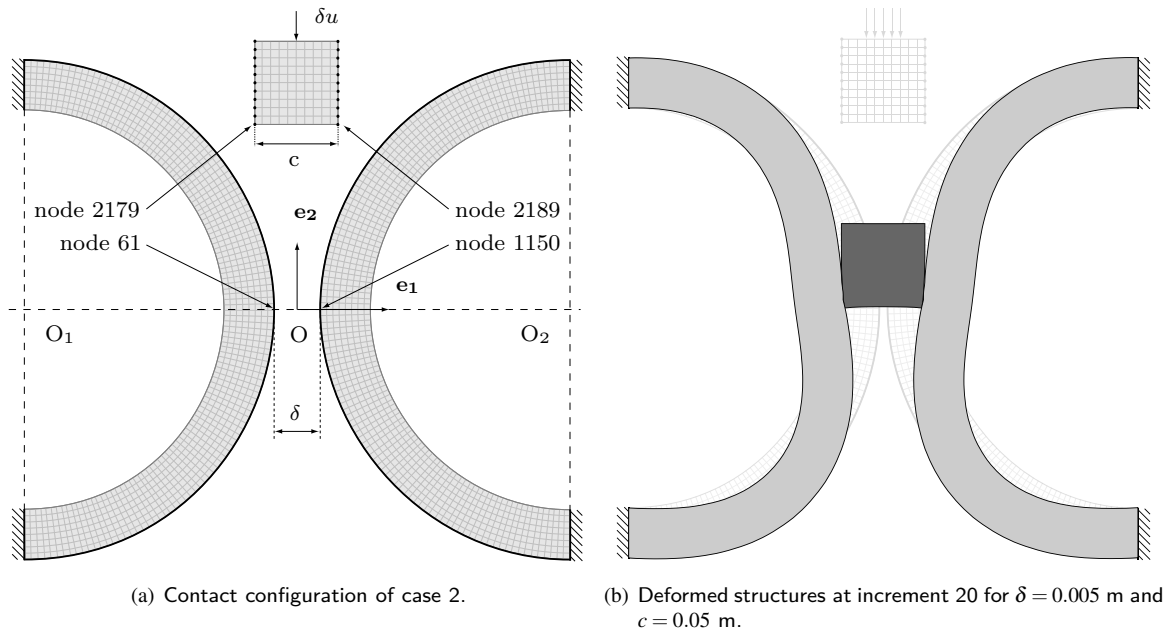


**Figure 18** – Case 2.

and two contact surfaces are taken into account: one on the outer edge of each half-ring. Accordingly, two sets of master nodes are defined on the edges of the square facing each half-ring. The assumption is made that no other node of the square may impact the half-rings.

The two half-rings are symmetric with respect to axis  $O\vec{y}$ , their outer radius is  $r_o = 0.15$  m and their inner radius is  $r_i = 0.12$  m. Obviously, the gap  $\delta$  between the half-rings is smaller than the length  $c$  of the square edge so that contact occurs.

Consistently with the mesh study made for test case 1, 120 finite elements are used over the circumference of each half-ring and 8 over their thickness. The square is meshed with 10 elements over each edge.

Finally, displacements along the axis  $-O\vec{y}$  are imposed on the middle node of the top edge of the square as depicted in Fig. 18(a).

### Conservation of symmetry

In the following:  $\delta = 0.005$  m and  $c = 0.05$  m, the Young modulus of the rings  $E_r$  is the double of the Young modulus of the square  $E_s$ :  $E_r = 2E_s$ . In this configuration, the square is hardly deformed during the simulation while repulsing the half-rings as pictured in Fig. 18(b).

The investigated contact configuration is symmetric with respect to axis  $O\vec{y}$  and it is expected to observe symmetric results in terms of displacements and contact forces with respect to the aforementioned axis of symmetry when a smoothing procedure is used<sup>8</sup>.

This is achieved by comparing displacements in the  $\vec{e}_2$  direction of node 61 belonging to the left ring and their symmetric counterparts on node 1150 belonging to the right ring.

Results show perfect symmetry of both displacements and contact forces for the two smoothing procedures of interest. For the sake of brevity, only the symmetry of displacements obtained with the B-spline smoothing method is depicted in Fig. 19.

### Results

In the following:  $\delta = 0.045$  m and  $c = 0.05$  m and the ratio between the Young moduli of the structures is  $E_r = 100E_s$ . In this configuration, the displacements of the nodes of the half-rings are negligible in comparison with those measured

<sup>8</sup>Symmetry of the results without smoothing procedures was already observed and is not recalled here for the sake of brevity.

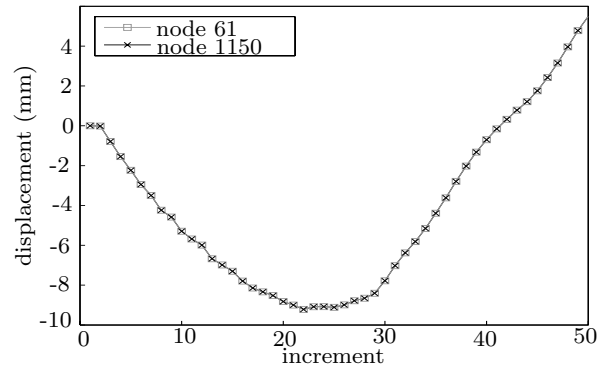


**Figure 19** – Displacement of nodes 61 and 1150 along  $\vec{e}_2$  obtained with the B-spline smoothing method.

on the square. Accordingly, the contact nodes of the square must slide on the contact surfaces and we expect to observe the effect of smoothing methods.

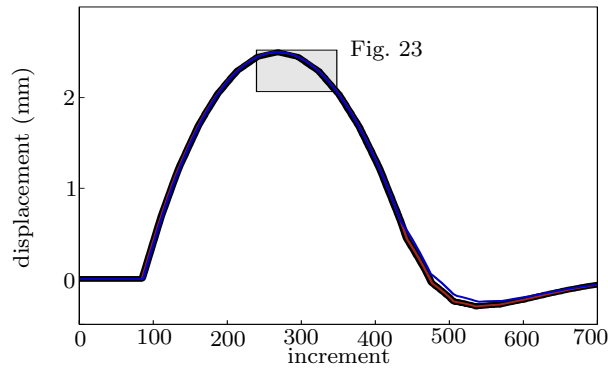


**Figure 20** – Displacement of node 2179 in the  $\vec{e}_1$  direction for linear mesh —, linear mesh with B-spline — and Hermite elements —.

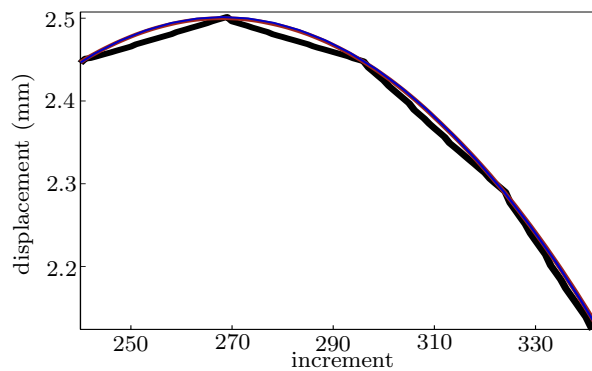


**Figure 21** – Displacement of node 2179 in the  $\vec{e}_1$  direction for linear mesh —, linear mesh with B-spline — and Hermite elements —.

Figures 20 and 21 picture the displacement of node 2179 during the simulation. Because the linear mesh is fine enough, no significant difference between linear mesh and smoothing methods is visible in Fig. 20. However, a zoom



on the curves over the contact phase – as in Fig. 21 – clearly highlights the improvements due to smoothing methods: the piecewise linear aspect of the results obtained with linear mesh, visible in Fig. 21, are replaced by a smooth displacement all along the contact surface.

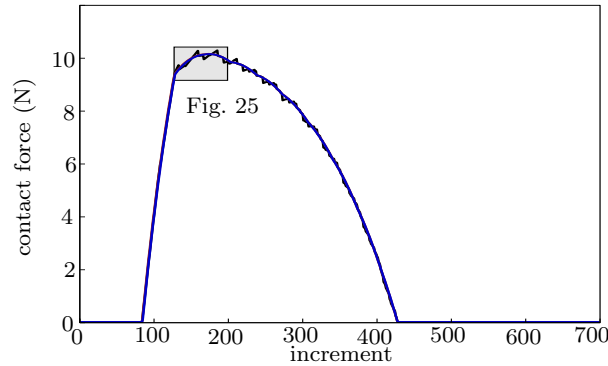


**Figure 22** – Norm of the contact force on node 2179 for linear mesh —, linear mesh with B-spline — and Hermite elements —.

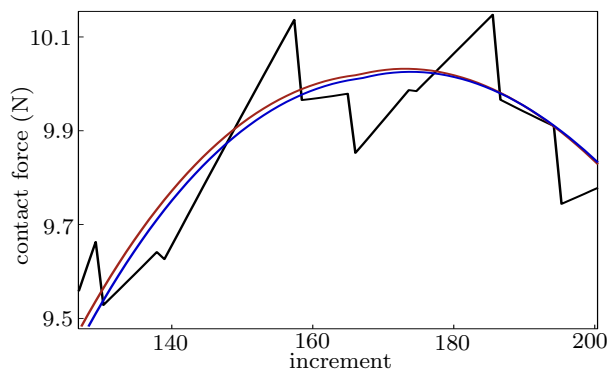


**Figure 23** – Norm of the contact force on node 2179 for linear mesh —, linear mesh with B-spline — and Hermite elements —.

One may notice in Fig. 20 that after the increment 450, the plotted displacement is piecewise linear for each of the three methods. The origin of this phenomenon does not lie in the contact solution algorithm itself but in the fact that the slave contact surface (the square) is defined with contact nodes. More precisely, contact between node 2179 of the square and the rings is lost around increment 440. Consequently, this node is not constrained anymore and his displacement is solely guided by the mechanical behaviour of the square. The changes of slope observed after increment 450 match the loss of contact for another node of the slave contact surface.

Similar results are obtained while looking at the contact forces on node 2179. These contact forces are smoothed with the use of B-splines or Hermite elements as depicted in Figs. 22 and 23.

The square and half rings contact case underlines the facetization issue associated with the use of a linear finite element mesh: displacements are piecewise continuous and contact forces are oscillating and discontinuous. While the imprecision over the computation of the displacements may be acceptable, the discontinuity of the contact force is much more troublesome. This is particularly true when contact forces are used for other computations such as, for instance, wear level and temperature variation.

### 4.3 case 3 :concentric rings

The third contact case of our study is similar to the one presented in [4]. Two concentric rings of equal thickness  $e = 0.75$  m are considered and pictured in Fig. 24 where the outer and the inner rings are respectively depicted in grey and white. The inner radius of the inner ring is  $r_i = 0.5$  m and the outer radius of the outer ring is  $r_o = 2$  m.

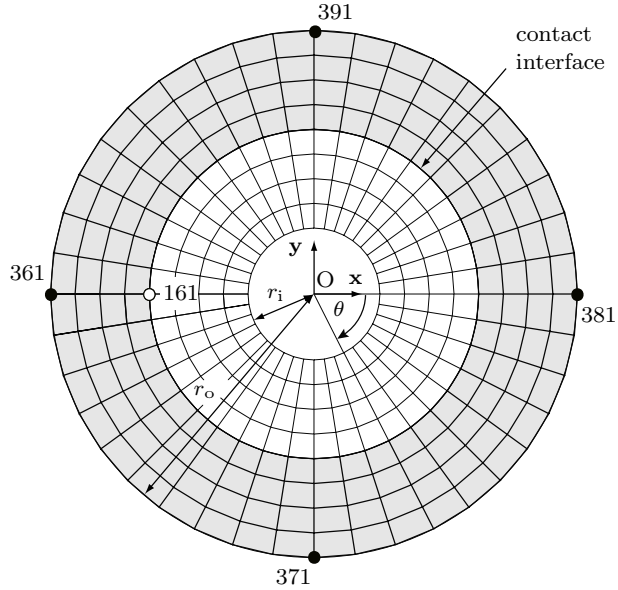


**Figure 24** – Finite element mesh of the two concentric rings (node 161 belongs to the inner ring).

Both rings are modeled with 160 four noded finite elements (Q4 or Hermite): 40 over the circumference and 4 along the thickness. The contact interface is defined as follows: the master contact surface is defined on the inner edge of the outer ring and the slave contact surface is defined on the outer edge of the inner ring. The outer radius of the inner ring is equal to the inner radius of the outer ring and meshing procedure is made in such a way that the contact nodes are exactly coincident with the nodes of the contact surface at the beginning of the simulation.

Also, in order to avoid rigid body motions and thus ill-conditioned matrices, taking into account the symmetry of the system, displacements of nodes 361 and 381 along the  $\vec{e}_2$  axis and displacements of nodes 371 and 391 along the  $\vec{e}_1$  axis are fixed to 0.

#### Displacement field continuity

A set of radial forces ( $\|\vec{F}\| = \sqrt{F_x^2 + F_y^2} = 10$  N) is applied on all the nodes of the outer radius of the outer ring while the inner ring is clamped on its inner radius. This way, it is possible to validate the results of the contact simulation by comparing them with the simulation of the radial compression of a single ring of inner radius  $r_i$  and outer radius  $r_o$ .

In total, four simulations are carried out with the same pressure field: (1) with a unique ring, (2) with two rings and a linearly discretized contact interface, (3) two rings and a B-spline used on the contact interface and (4) two rings with Hermite elements used for the modeling of master structure, meaning the outer ring.

Displacement fields obtained for each simulation are depicted in Figs. 25(a), 25(b), 25(c) and 25(d). One may notice the great similarity between Figs. 25(a), 25(d) and 25(c) highlighting the continuity of the displacement field between the two rings when a B-spline or Hermite elements<sup>9</sup> are used on the contact interface. To the contrary, when the contact interface is linearly discretized, the displacement field – pictured in Fig. 25(b) – loses both symmetry and continuity at the interface.

<sup>9</sup>One may notice that the color field depicted in Fig. 25(d) is smoother than the ones depicted in the other figures. This is both the consequence of a different way to plot the color field (imposed by the structure of the results data) and the use of cubic shape functions with Hermite elements. If linear finite element meshes had been finer, similar color fields may have been obtained with a unique ring or with B-splines respectively in Figs. 25(a) and 25(c).

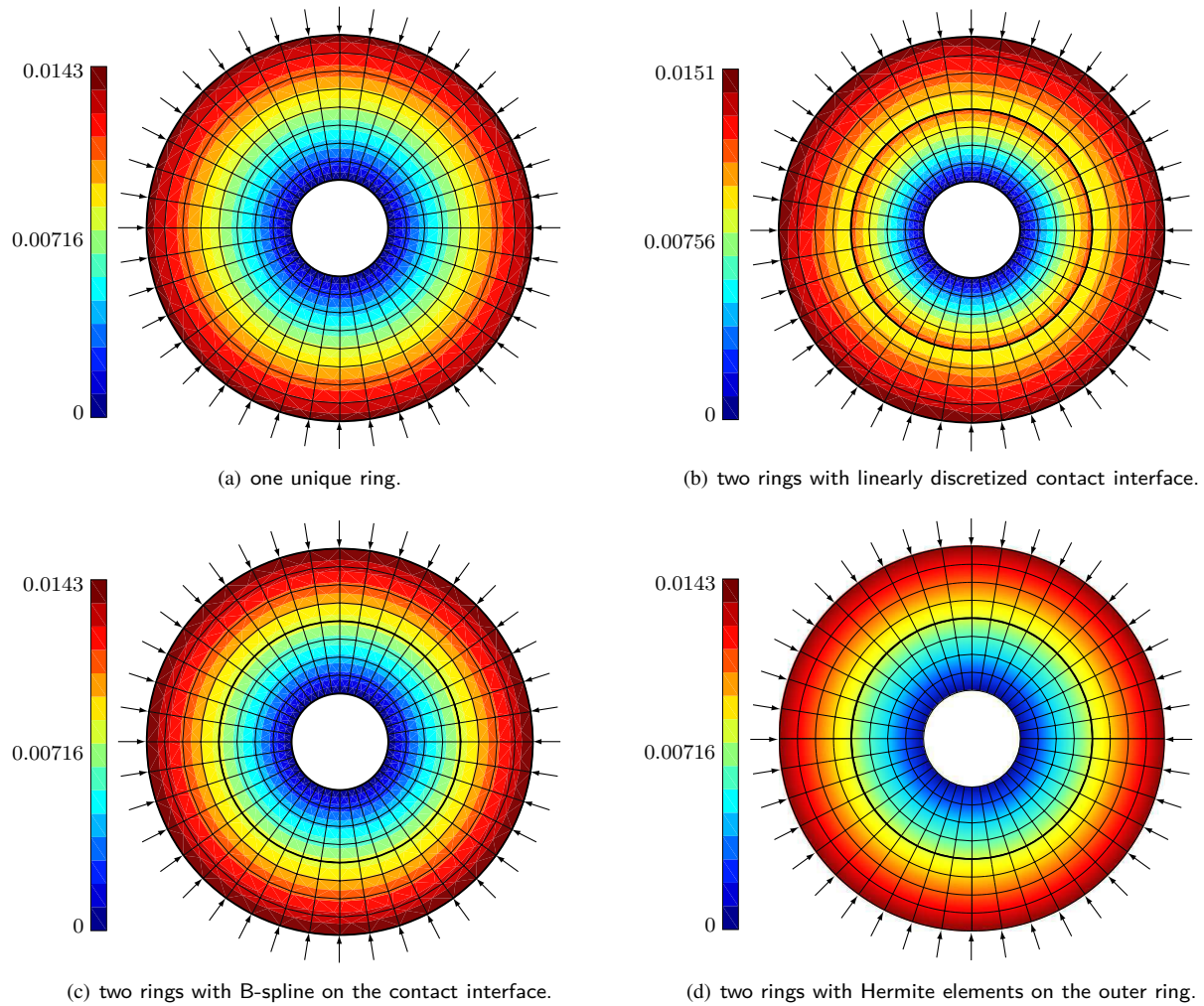


**Figure 25** – Displacement fields obtained for different configurations with an identical radial pressure field.

Interestingly, this contact case allows to show the improvements due to the use of smoothing methods with respect to usual linear finite element meshes even when no large sliding occur between structures. An evolution of this contact case consists precisely in adding large sliding thanks to the rotation of the inner ring which is the focus of the next section.

### Rotation of the inner ring

The inner ring is not clamped anymore and displacements are imposed on the nodes belonging to its inner edge so that it rotates around the axis  $Oz$  of an angle  $\theta = \pi$ .

While the inner ring rotates, the radial forces set described in the previous section is applied on the outer ring all along the simulation. Due to the progressive application of this external loading, contact forces on the interface increase over the first increments of the simulation and then stabilize around an equilibrium value  $F_c$  on each node of the interface.

The study configuration is axi-symmetric and it is of great interest to ensure that contact forces are uniformly distributed along the contact interface.

In order to assess the uniformity of the contact forces distribution along the contact interface, contact forces are computed on each node of the contact interface belonging to the inner ring over the simulation. The focus is made on

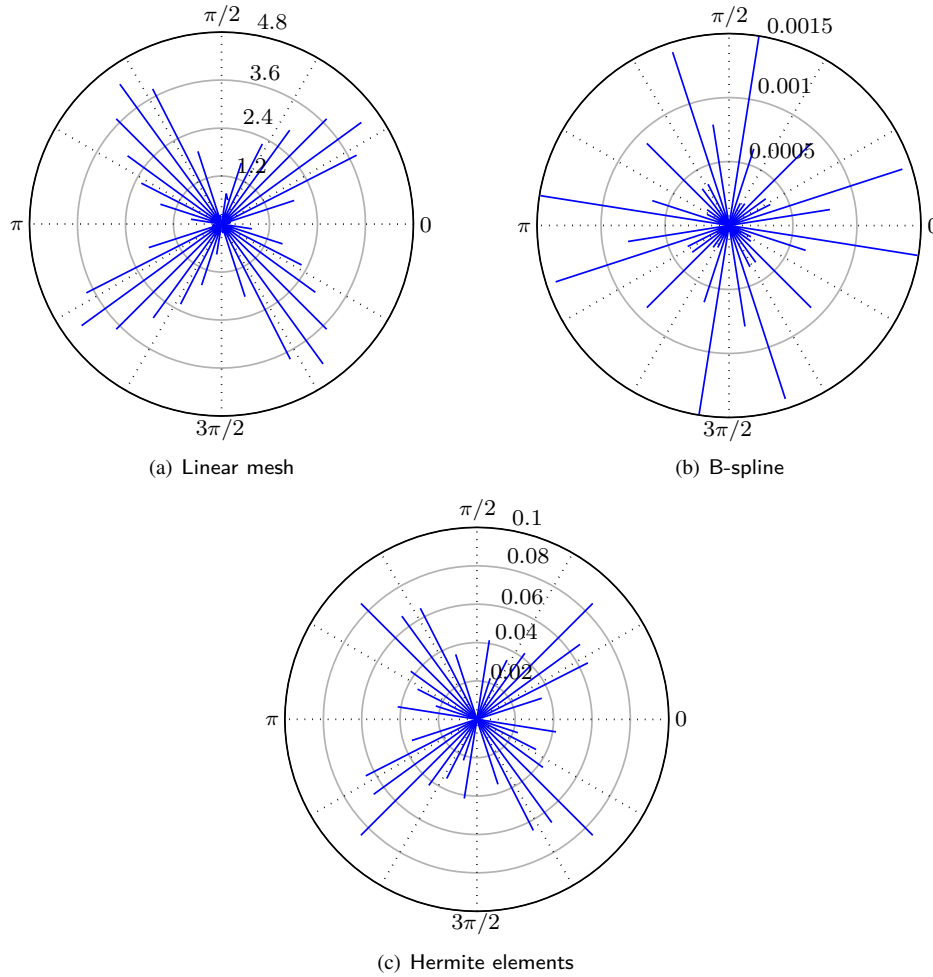


**Figure 26** – Distribution of the contact force along the contact interface, variation in % with respect to  $F_e$ .

the variation (in %) of the norm of each contact force with respect to the equilibrium value  $F_e$  aforementioned.

The maximum error is found at increment 220 (over 1000) and the associate contact distribution is depicted in Figs. 26(a), 26(b) and 26(c) respectively for a linear mesh, a linear mesh with B-spline and Hermite elements. One may notice the different scales used on each figure: while the variation with respect to  $F_e$  on the contact interface may vary up to 4.8 % when no smoothing method is used, the maximum variation is about 0.0015 % with B-splines and 0.1 % with Hermite elements.

These results are consistent with the break of symmetry observed in Fig. 25(b) when a linear mesh is used. Contact forces all over the simulation on node 161 are pictured in Fig. 27. Significant differences arise between the linear mesh and the smoothing methods: non smoothness of the contact forces while the node rotates on the contact interfaces is highlighted.

While the use of B-spline or Hermite elements allow to obtain smooth contact forces, it is noticeable in Fig. 27 that results obtained with Hermite elements vary significantly during the simulation. This variation appears to be periodic and its periodicity matches the size of an element, which is easily identifiable thanks to the linear mesh curve.

In order to understand the origin of these variations we focus on the shape of the master contact surface (the inner edge of the outer ring) for two increments  $i_1$  and  $i_2$  mentioned in Fig. 27. At increment  $i_1$ , results with B-splines and Hermite elements match perfectly while the gap between these two methods is maximum at increment  $i_2$ .

Contact surface is partially represented in Figs. 28(a) and 28(b) respectively at increments  $i_1$  and  $i_2$ . At increment

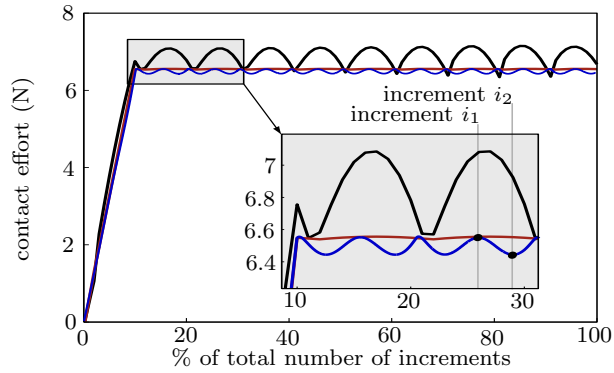


**Figure 27** – Contact force on node 161 of the inner ring: linear mesh —, linear mesh with B-spline — and Hermite elements —.

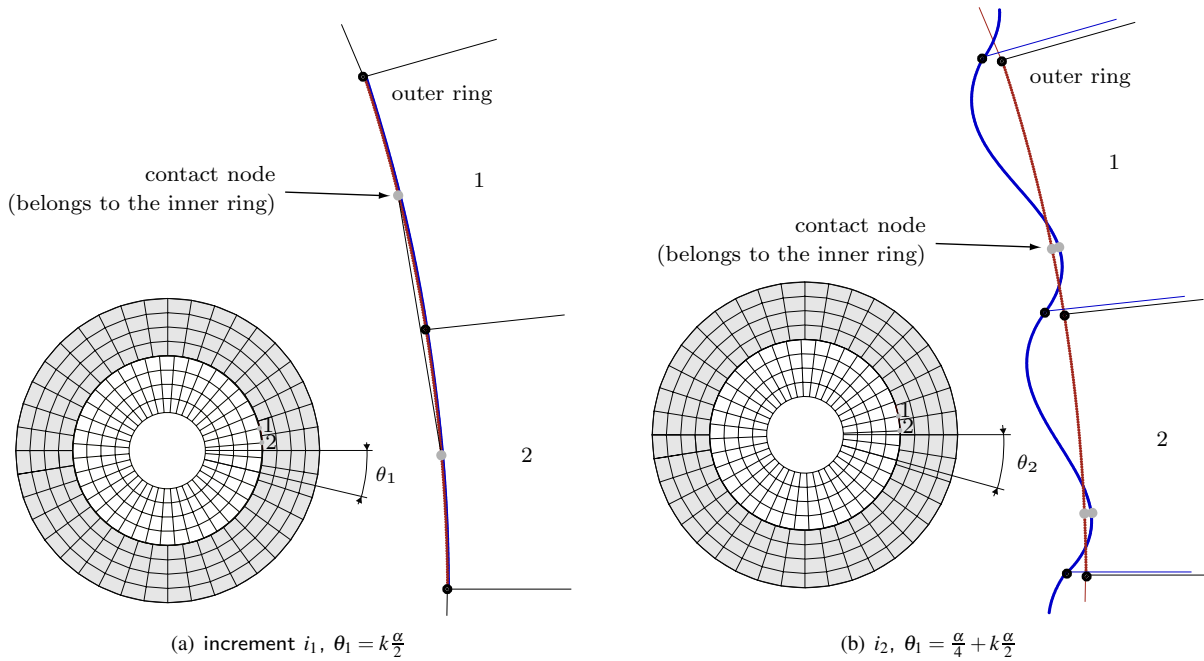


**Figure 28** – Contact surface (displacements are magnified for the sake of visibility) for two increments for linear mesh and B-spline — and for Hermite elements —.

$i_1$  – where results between the two smoothing methods match perfectly – one may see in Fig. 28(a) that the two contact surfaces (B-splines and Hermite) are indistinguishable. It is noticeable in Fig. 27 that this perfect match happens twice while the contact node moves along an obstacle element: (1) when the contact node is at the middle of the obstacle element as depicted in Fig. 28(a) and (2) when the contact node is facing a node of the obstacle element. Accordingly, these results underline a different behaviour between the two smoothing methods when a contact node moves along the rest of the obstacle element as pictured in Fig. 28(b).

At increment  $i_2$  – where the gap between the two smoothing methods is maximum – the contact surfaces are clearly distinct. Interestingly, the contact surface obtained with Hermite elements undulates (the scale of undulation is highly amplified in Fig. 28(b) for the sake of visibility).

This phenomenon is a consequence of the mechanical behaviour of the Hermite element exhibited in section 3.2 where it is shown that a punctual force applied on one of its edges leads to a significant rotation of the tangent vectors

around the nodes of this edge. This undulation varies while the contact point moves along the edge when the inner rings rotates. Contrary to intuitive ideas, this phenomenon does not reveal a limitation of Hermite elements for contact problems. Indeed, the node-to-segment contact formulation is dissymmetric. In this context, the contact case presented in this section is actually comparable to a bladed-disk/casing contact case where several beams (modeling the blades) would impact the outer ring on a few distinct areas. Accordingly, the results obtained with Hermite elements precisely reflect this limitation associated with the contact algorithm. In the case of the combination of linear elements with a B-spline, this dissymmetry is somehow filtered due to the low order of the linear element formulation that is the reason why results are in better agreement with the continuous problem solution.

In order to get closer from the initial problem with Hermite elements, one solution may be to increase the number of contact nodes per obstacle element to avoid the oscillation of the contact surface. In order to do so, it is possible to use a finer mesh for the inner ring, or a smaller number of elements <sup>10</sup> over the circumference of the outer ring. This last possibility – the only one leading to acceptable computation times when considering the Hermite elements formulation used in our study – does not provide satisfying results due to the outbreak of non-negligible geometrical approximations when 10 Hermite elements are considered as depicted in Fig. 29. When 20 Hermite elements are used over the circumference of the outer ring, the amplitude of the oscillations is reduced but there is no improvement relatively to the initial configuration.

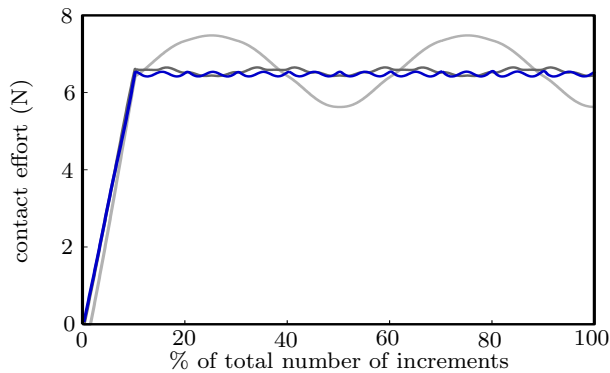


**Figure 29** – Contact force on node 161 of the inner ring with a variable number of Hermite elements on the circumference of the outer ring: 10 Hermite elements —, 20 Hermite elements — and 40 Hermite elements —.

Were a finer mesh to be considered for the inner ring, the additional degrees of freedom inherent to Hermite elements would lead to time consuming simulations. In order to avoid cumbersome computation times, one may consider using specifying meshing methods – such as the octree method that allows for a less fine mesh within the structure – or specific finite elements such as those introduced in [40] for which  $C^1$ -continuity is ensured on one edge only thus reducing the number of additional degrees of freedom.

## 5 Conclusion

This study focuses on the presentation and application of two smoothing methods – the computation of a B-spline over a finite element mesh and the use of high order finite elements such as Hermite elements – for the solution of contact problems involving large slidings. While both methods advantageously tackle the facetization issue inherent to the use of linear finite element meshes, they are very different in nature and thus may be considered for different types of applications.

It is first shown that each method leads to significant improvements in terms of geometrical representation of the contact surfaces in comparison with linear, quadratic and cubic finite element meshes. Beside of ensuring a reduction of the discretization error for curved profiles – even when a small number of elements is considered – both methods ensure the continuity of the normal vector to the contact surface when sliding from an element to another.

<sup>10</sup>In this case, the forces applied on the outer ring are computed through the integration over the circumference of the ring of a pressure equivalent to the initial radial forces. This way, a good repartition of the forces as well as an accurate deformation of the outer ring are ensured.



The good compatibility of the two smoothing methods with the contact algorithm of interest – based on the bi-potential method – is explained and only the detection procedure must be updated. Results given for different contact cases with large slidings emphasize the enhancements in terms of numerical stability as well as the higher precision of the contact forces computed. Using Hermite elements lead to results particularly consistent with a node-to-segment approach and thus highlight the limitations of such a formulation. Indeed, contact surface undulations mentioned in section 4.3 that may be observed do not stem from geometrical imprecision: they underline the fact that a richer contact formulation is required for an accurate modeling of the continuous contact problem involving two concentric rings.

While geometric patches seem particularly relevant when the finite element mesh may not be modified – for instance in the case of an industrial procedure – it appears that Hermite elements allow for a higher level of precision and results reflect very consistently the chosen contact formulation.

## References

- [1] Fischer, K. A., and Wriggers, P., 2006. “Mortar based frictional contact formulation for higher order interpolation using moving friction cone”. *Computer methods in applied mechanics and engineering*, **195**, pp. 5020–5036. 1, 4
- [2] McDevitt, T. W., and Laursen, T. A., 2000. “A mortar-finite element formulation for frictional contact problems”. *Int. J. Numer. Methods Engrg.*, **48**, pp. 1525–1547. 1, 4
- [3] Puso, M. A., and Laursen, T. A., 2004. “A mortar segment-to-segment contact method for large deformation solid mechanics”. *Comput. Methods Appl. Mech. Engrg.*, **93**, pp. 601–629. 1, 4
- [4] Belytschko, T., Daniel, W. J. T., and Ventura, G. K., 2002. “A monolithic smoothing-gap algorithm for contact impact based on the signed distance function”. *Int. J. Numer. Methods Engrg.*, **55**, pp. 101–125. 1, 2, 4, 25
- [5] Legrand, M., 2005. “Modèles de prediction de l’interaction rotor/stator dans un moteur d’avion”. Thèse de doctorat (phd thesis), École Centrale de Nantes, Nantes, France. 1, 4
- [6] Kikuchi, N., 1982. “Penalty/finite element approximations of a class of unilateral contact problems”. *Penalty Method and Finite Element Method*. ASME: New York. 1, 4
- [7] Muñoz, J. J., 2008. “Modelling unilateral frictionless contact using the null-space method and cubic B–Spline interpolation”. *Computer methods in applied mechanics and engineering*, **197**, pp. 979–993. 1, 4
- [8] Wriggers, P., and Krstulovic-Opara, 2000. “On smooth finite element discretization for frictional contact problems”. *J. Appl. Math. Mech. (ZAMM)*, **80**, pp. 77–80. 1, 4
- [9] Hughes, T. J. R., A., C. J., and Y., B., 2005. “Isogeometric analysis : CAD, finite elements, nurbs, exact geometry and mesh refinement”. *Computer Methods in Applied Mechanics and Engineering*, **194**, pp. 4135–4195. 1, 4
- [10] Temizer, I., Wriggers, P., and Hughes, T. J. R., 2011. “Contact treatment in isogeometric analysis with nurbs”. *Computer Methods in Applied Mechanics and Engineering*, **200**, February, pp. 1100–1112. 1, 4, 10
- [11] de Lorenzis, L., Temizer, I., Wriggers, P., and Zavarise, G., 2011. “A large deformation frictional contact formulation using NURBS-based isogeometric analysis”. *International Journal for Numerical Methods in Engineering*. 1, 4, 10
- [12] Feng, Z. Q., Joli, P., Cros, M., and Magnain, B., 2005. “The bi-potential method applied for the modeling of dynamic problems with friction”. *Computational Mechanics*, **36**, pp. 375–383. 1, 4, 5, 7
- [13] Armero, F., and Petöcz, E., 1998. “Formulation and analysis of conserving algorithms for dynamic contact/impact problems”. *Computer Methods in Applied Mechanics and Engineering*, **158**, pp. 269–300. 1, 4
- [14] Arora, J. S., Chahande, A. I., and Paeng, J. K., 1991. “Multiplier methods for engineering optimization”. *International Journal for Numerical Methods in Engineering*, **32**, pp. 1485–1525. 1, 4

- [15] Hughes, T. J. R., Taylor, R. L., Sackman, J. L., Curnier, A., and Kanoknukulchai, W., 1976. “A finite element method for a class of contact-impact problems”. *Computer Methods in Applied Mechanics and Engineering*, **8**, pp. 149–276. 1, 4
- [16] Simo, J. C., and Laursen, T. A., 1992. “An augmented lagrangian treatment of contact problems involving friction”. *Computers & Structures*, **42**(1), pp. 97–116. 1, 4
- [17] Alart, P., and Curnier, A., 1991. “A mixed formulation for frictional contact problems prone to newton like solution methods”. *Computer methods in applied mechanics and engineering*. 1, 4
- [18] de Saxcé, G., and Feng, Z. Q., 1991. “New inequality and functional for contact with friction : the implicit standard material approach”. *Mechanics of structures and machines*. 1, 4, 7
- [19] Legrand, M., Batailly, A., Magnain, B., Cartraud, P., and Pierre, C., 2012. “Full three-dimensional investigation of structural contact interactions in turbomachines”. *Journal of Sound and Vibration*, **331**, pp. 2578–2601. 1, 4, 10
- [20] Batailly, A., Legrand, M., Millecamps, A., and Garcin, F., 2012. “Numerical-experimental comparison in the simulation of rotor/stator interaction through blade-tip/abradable coating contact”. *Journal of Engineering for Gas Turbines and Power*, **in press**. 1, 4
- [21] Schmiechen, P., 1997. “Travelling wave speed coincidence”. PhD thesis, Imperial College of Science, Technology and Medicine - University of London. 4
- [22] Legrand, M., Pierre, C., Cartraud, P., and Lombard, J. P., 2009. “Two-dimensional modeling of an aircraft engine structural bladed disk-casing modal interaction”. *Journal of Sound and Vibration*, **319**(1-2), pp. 366–391. 4
- [23] Batailly, A., Legrand, M., Cartraud, P., and Pierre, C., 2010. “Assessment of reduced models for the detection of modal interaction through rotor stator contacts”. *Journal of Sound and Vibration*, **329**, pp. 5546–5562. 4
- [24] Padova, C., Barton, J., Dunn, M., and Manwaring, S., 2007. “Experimental results from controlled blade tip/shroud rubs at engine speed”. *Journal of Turbomachinery*, **129**, pp. 713–723. 4
- [25] Stadler, M., Holzapfel, G. A., and Korelc, J., 2003. “ $C^n$  continuous modelling of smooth contact surfaces using NURBS and application to 2D problems”. *International Journal for Numerical Methods in Engineering*, **57**, pp. 2177–2203. 5
- [26] Signorini, A., 1959. “Questioni di elasticità non linearizzata e semilinearizzata (issues in nonlinear and semilinear elasticity)”. *Rendiconti di Matematica e delle sue applicazioni*, **18**, pp. 95–139. 6
- [27] Francavilla, A., and Zienkiewicz, O. C., 1975. “A note on numerical computation of elastic contact problems”. *International Journal for Numerical Methods in Engineering*, **9**, pp. 913–924. 7
- [28] Sachdeva, T. D., and Ramarkrishnan, C. V., 1981. “A finite element solution for the two-dimensional elastic contact problems with friction”. *International Journal for Numerical Methods in Engineering*, **17**, pp. 1257–1271. 7
- [29] Sachdeva, T. D., Ramarkrishnan, C. V., and Natarajan, R., 1981. “A finite element method for the elastic contact problems”. *Transaction of the ASME*, **103**, pp. 456–461. 7
- [30] Zienkiewicz, O. C., and Taylor, R. L., 2000. *The finite element method - Volume 2 : Solid Mechanics*. Butterworth-Heinemann. 7
- [31] de Saxcé, G., and Feng, Z. Q., 1998. “The bi-potential method : a constructive approach to design the complete contact law with friction and improved numerical algorithms”. *Mathematical and computer modeling*. 7
- [32] Magnain, B., 2006. “Développement d’algorithmes et d’un code de calcul pour l’étude des problèmes de l’impact et du choc”. Thèse de doctorat (phd thesis), Université d’Évry-Val d’Essonne, Évry, France. 7



- [33] Ulaga, S., Ulbin, M., and Flasker, J., 1999. “Contact problems of gears using overhauser splines”. *International Journal of Mechanical Sciences*, **41**, pp. 385–395. [10](#)
- [34] Al-Dojayli, M., and Meguid, S. A., 2002. “Accurate modeling of contact using cubic splines”. *Finite Elements in Analysis and Design*, **38**, pp. 337–352. [10](#), [20](#)
- [35] Piegl, L. A., and Tiller, W., 2003. “Circle approximation using integral b-splines”. *Computer-Aided Design*, **35**, pp. 601–607. [10](#)
- [36] de Boor, C., 1993. *B(asic)-Spline Basics in Fundamental Developments of Computer-Aided Geometric Modeling*. (Piegl L., ed.) Academic Press, Washington D.C. [10](#)
- [37] Arnoult, E., 2000. “Modélisation numérique et approche expérimentale du contact en dynamique: application au contact aubes/carter de turboréacteur”. PhD thesis, Université de Nantes. [12](#)
- [38] Plass, M., and Stone, M., 1983. “Curve-fitting with piecewise parametric cubics”. *Computer Graphics*, **17**(3). [12](#)
- [39] El-abbasi, N., Meguid, S. A., and Czekanski, A., 2001. “On the modelling of smooth contact surfaces using cubic splines”. *Int. J. Numer. Methods Engrg.*, **50**, pp. 953–967. [20](#)
- [40] Sauer, R. A., 2011. “Enriched contact finite elements for stable peeling computations”. *International Journal for Numerical Methods in Engineering*, **87**, pp. 593–616. [29](#)